M.Sc. Environmental Physics

Master Thesis

On Uncertainties in Forecasting Regions Where Persistent Contrails Can Occur

Victor Leon von Koslowski

Matriculation number: 6014726

Date of birth: August 3rd, 1996

Deutsches Zentrum für Luft- und Raumfahrt

Universität Bremen

Abstract

Rerouting air traffic to avoid ice super saturated regions (ISSRs) where contrails can persist for several hours has the potential to significantly reduce the overall climate impact of aviation. Besides operational considerations, e.g., air traffic control and airspace capacity, one of the main challenges in employing such a strategy is that numerical weather prediction (NWP) models struggle to accurately forecast ISSRs. In this thesis, the robustness of ISSR forecasts is investigated by comparing the potential of persistent contrails (PPC, a binary value that indicates whether persistent contrails can form) fields of a deterministic run of the ICON (Icosahedral non-hydrostatic) NWP model with the PPC field averaged over 40 ensemble forecasts, PPC_{prob}. The median of the conditional distribution f(PPC_{prob} | PPC = 1) was used as a proxy for the robustness of the ISSR forecasts. The median f(PPC_{prob} | PPC = 1) displays a seasonal pattern with lower values, i.e., less robust forecasts, in the summer months and higher values, i.e., more robust values, in the winter months. From the annual cycle of the median f(PPC_{prob} | PPC = 1), the ten days with the highest (robust days) and lowest median f(PPC_{prob} | PPC = 1) (non-robust days) were chosen to investigate the synoptic situation in more detail. The robust days exhibit stronger horizontal wind and ISSRs that coincide with more active uplifting. The non-robust days are characterized by weaker horizontal wind speeds and smaller horizontal scales. Backwards Lagrangian trajectories calculated from ERA5 reanalysis data on the selected days reveal that ice supersaturation was mostly driven by cooling on the robust days and mixing on the non-robust days. These findings suggest that the main formation mechanism for ISSRs on the robust days are large-scale lifting processes that occur in the vicinity of frontal systems, while on the non-robust days, deep convective activity in the hours and days before the considered event is the source of ISSRs in the upper troposphere. Further research is required to investigate the link between deep convective systems and the robustness of ISSR forecasts. For the implementation of operational contrail avoidance strategies, it could be beneficial to deploy such strategies in the winter months, when the forecast is more robust, and the overall air traffic volume is lower.

Acknowledgements

I would like to express my sincere gratitude to Prof. Dr. Annette Ladstätter-Weißenmayer and Prof. Dr. Anja Schmidt for supervising this thesis and their support. I would also like to thank Prof. Dr. Anja Schmidt, for making me feel welcome from the very first day at her department at the DLR. It was an absolute pleasure working at the Institute of Atmospheric Physics.

This thesis would not have been possible without the incredible support from my advisor, Dr. Klaus Gierens, and his patience in explaining things to me in detail, his flexibility regarding my schedules and the countless pleasant and inspiring conversations that we had.

I am also grateful to Dr. Sina Hofer for her guidance on data processing and analysis and helping me get settled at the DLR. Thank you to Dr. Arnold Tafferner of WxFUSION for providing data on summertime convective situations. I also want to acknowledge the entire faculty at the PEP program and Anja Gatzka from the University of Bremen for their continuous support throughout the years during my studies.

I am deeply thankful to my parents and my sister, Rebecca, for everything that they have made possible for me and for always believing in me and encouraging me to follow my dreams.

Finally, I am immensely grateful to my partner, Isabella, for her unconditional support in achieving all my goals, her patience and flexibility, for always believing in me, and for picking me up whenever I feel down.

This thesis was a very long time in the making, and it would not have been possible without those mentioned above. Thank you.

Table of contents

1. Introduction 5
2. Theoretical Background 7
  2.1. Water Vapor in the Atmosphere 7
  2.2. Contrail Formation 9
  2.3. Synoptic Meteorology and Ice Supersaturation 11
3. Data 13
  3.1. WAWFOR Data (Experimental Data Set Klima 1) 13
  3.2. Icon NWP Output 15
  3.3. ERA5 Reanalysis Data 15
  3.4. Meteorological Data 16
4. Research Methods 17
  4.1. Conditional Distribution of PPC_{prob} where PPC = 1 17
  4.2. Mean Contrail Length 18
  4.3. Receiver Operating Characteristics 19
  4.4. Autocorrelation Scales of Selected Meteorological Properties 21
  4.5. Treatment of Meteorological Variables 22
  4.6. Lagrangian Trajectories 24
5. Results 26
  5.1. Conditional Distribution of PPC_{prob} where PPC = 1 26
  5.2. Mean Contrail Length 29
  5.3. Receiver Operating Characteristics 30
  5.4. Autocorrelation of Vertical Velocities 32
  5.5. Synoptic Situation on the Selected Days 34
  5.6. Lagrangian Trajectories 36
6. Discussion 40
  6.1. Criterion for the Choice of the Robust and Non-robust Days 40
  6.2. Synoptic Situation on the Selected Days 42
  6.3. Vertical Velocity Field on the Selected Days 44
7. Conclusion and Outlook 48
References 52
List of Figures 56
List of Tables 60

1. Introduction

Global air transport contributes to climate change by both the emission of CO_2, which amounts to approx. 2.5% of annual anthropogenic CO_2 emissions, and the so-called non-CO_2 effects that occur due to the emission of other species, e.g., NO_x, water vapor and soot, and the formation of persistent condensation trails (contrails, IEA, 2025; Lee et al., 2021). The effective radiative forcing (ERF), a metric used to assess the climate impact of perturbations in the atmosphere, of the non-CO_2 effects is approx. twice as high (66.6 mW m^{-2}) as the ERF due to aviation's CO_2 emissions (34.3 mW m^{-2}; Lee et al., 2021; Myhre et al., 2014). Of all non-CO_2 terms, cirrus contrails are estimated to have the largest warming effect with an ERF of 57.4 mW m^{-2}, although there are large uncertainties in the exact numerical value (Lee et al., 2021).

While individual contrails can have a cooling effect by reflecting incoming solar radiation, the majority of contrails (approx. 90%) has a warming effect by absorbing and re-emitting outgoing longwave radiation (Wilhelm et al., 2021). Even though commercial airliners spend approximately 15% of their cruise portion in ice-supersaturated regions (ISSRs), there is evidence that only a small portion of all flights is responsible for a majority of the warming due to contrail and contrail cirrus (Gierens, 2010; Teoh et al., 2020). Identifying and avoiding ISSRs in which persisting contrails with a high warming potential can form therefore has the potential to significantly reduce the overall climate impact of aviation.

Although trials have shown that contrails can be mitigated by vertically deviating air traffic on a small-scale and in low-traffic scenarios, there are currently no large-scale operational procedures in place to mitigate contrails by rerouting air traffic to avoid ISSRs (Sausen et al., 2024). This is because rerouting flights is complex due to airspace and air traffic control capacities as well as safety considerations, e.g., the circumnavigation of thunderstorms and turbulence regions (Sausen et al., 2024). Additionally, diverting flights from their optimum trajectory entails fuel penalties, so the trade-off between higher emissions of CO_2 and all other species and resulting higher costs for the airlines and the reduced ERF due to mitigated contrail cirrus must be weighed against another. Finally, deviating flights requires knowledge about when and where contrails will form precisely, which requires an accurate weather forecast. Unfortunately, predicting regions where persistent contrails occur still poses a challenge for numerical weather prediction (NWP) models, in particular because of difficulties in forecasting ice super saturation (von Bonhorst et al., 2025; Hofer et al., 2024).

The goal of this research project is to investigate the robustness in the forecasts of ISSRs using results from the ICON numerical weather prediction model (NWP) and to ultimately contribute to the development of operational contrail mitigation strategies. Generally, a numerical weather forecast is considered as robust if the model gives similar results when forced with slightly different initial conditions. In this study, robustness is measured by comparing the results of ensemble experiments with the deterministic experiment.

Specifically, this thesis aims at answering the following questions:

1. Are there any synoptic situations during which the forecast of ISSRs is especially robust or not?
2. Are there any synoptic situations where one can confidently say that the application of operational contrail avoidance strategies (e.g., rerouting air traffic to avoid ISSRs) is particularly beneficial to the overall climate impact of aviation?
3. Which (if any) practical conclusions can be drawn for possible contrail avoidance strategies for flight dispatchers and pilots?

2. Theoretical Background

2.1. Water Vapor in the Atmosphere

Water vapor in the atmosphere is the most abundant natural greenhouse gas (GHG), but, unlike CO_2 and other GHGs, its concentration is not mainly controlled by anthropogenic emissions but by air temperature (Stocker, 2014). Besides being a natural GHG, water occurs in the atmosphere in all three phases (solid, liquid and gaseous) and plays a key role in weather and climate by, e.g., the release or absorbing of latent heat during phase changes and through precipitation (Gierens et al., 2012; Wallace & Hobbs, 2006).

Saturation is an equilibrium state at which the rate of evaporation balances the rate of condensation over a flat surface of water (or ice, Gierens et al., 2012). The partial pressure of water vapor at saturation, saturation vapor pressure, e_s, only depends on the temperature T and this dependence is given by the Clausius-Clapeyron equation:

$$\frac{d \ln e_s}{dT} = \frac{L}{RT^2}$$

where L is the latent heat of evaporation or sublimation and R is the universal gas constant (Gierens et al., 2012). Due to the different molecular structures of water and ice, the saturation vapor pressure curves over water and ice differ, with the saturation pressure over ice always being lower than that over water because more energy is required for water molecules to break out of the crystalline ice structure (Gierens, 2010).

There are different physical parameters to describe water vapor in the atmosphere (Wallace & Hobbs, 2006). Specific humidity, q, is defined as the ratio between the mass of water vapor in an air parcel to the total mass of that air parcel:

$$q = \frac{m_v}{m_v + m_d}$$

where m_v is the mass of water vapor and m_d is the mass of dry air in an air parcel (Wallace & Hobbs, 2006). Humidity can also be expressed in relative humidity (RH), which is defined as the ratio of actual water vapor pressure, e, over saturation vapor pressure, e_s, expressed in percent (Gierens et al., 2012):

$$RH = \frac{e}{e_s} * \ 100\%$$

Relative humidity is preferred for many applications in meteorology because it takes on values that are more intuitive and independent of temperature and density, while specific humidity varies by several orders of magnitude between the surface level and the tropopause (Gierens et al., 2012). In particular, cloud formation and dissipation (also for contrails) are controlled by RH rather than absolute humidity (Wallace & Hobbs, 2006). Vapor concentrations can reach relative humidity values below (subsaturation) or above (supersaturation) 100%. In these unstable solutions, evaporation or sublimation (in the case of subsaturation) or condensation (in the case of supersaturation) are the processes moving the vapor concentration towards an equilibrium (i.e., saturation, where RH is 100%, Gierens et al., 2012). In the troposphere, condensation nuclei are abundant and typically, water vapor is only supersaturated with respect to water by a few percent in clouds (Wallace & Hobbs, 2006). On the other hand, supersaturation w.r.t. ice can reach higher values due to the special crystalline structure of ice (Gierens, 2010).

2.2. Contrail Formation

The Schmidt-Appleman criterion (SAC) states that for the formation of contrails, condensation of the emitted water vapor must take place during the mixing of an aircraft's hot exhaust with cold ambient air (see Figure 1; Gierens, 2010). Due to the abundance of particles in the exhaust plume, contrail formation is not controlled by the number of condensation nuclei. Instead, the formation of contrails is a thermodynamic process that depends on multiple factors: the overall propulsion efficiency η, the specific fuel energy content Q (Q ≈ 43 MJ kg^{-1}), the specific emission of water vapor EI_{H2O} (EI_{H2O} ≈ 1.25 kg water per kg fuel burnt) and the ambient temperature and humidity (Gierens, 2010). Schumann (1996) summarized these in the following formula:

$$G = \frac{de}{dT} = \frac{EI_{H20}\ p\ c_p}{\epsilon\ Q\ (1-\eta)}$$

where ϵ = 0.622 is the molar mass ratio of water and air, c_p is the specific heat capacity of air at constant pressure, e is the water vapor partial pressure and T the temperature of the plume.

When plotted in an e-T-diagram, G represents the slope of mixing trajectories, i.e., the temperature and water vapor partial pressure that an air parcel from an exhaust plume take during the mixing with ambient air (see Figure 1). The requirement for contrail formation implies that the mixing trajectories pass through the area that is supersaturated w.r.t. liquid water. Only then will liquid water droplets condensate on the particles of the exhaust plume. After their initial formation, the liquid droplets will freeze quickly at ambient temperatures below -38°C (Gierens, 2010).

The prerequisite for contrails to persist over hours (rather than evaporate within seconds to minutes after their formation) and ultimately spread into cirrus layers is ice-supersaturation in the ambient atmosphere (Gierens, 2010). Only in ISSRs are the conditions sufficiently cold and humid to support further growth of ice crystals after the initial contrail formation (Gierens, 2010).

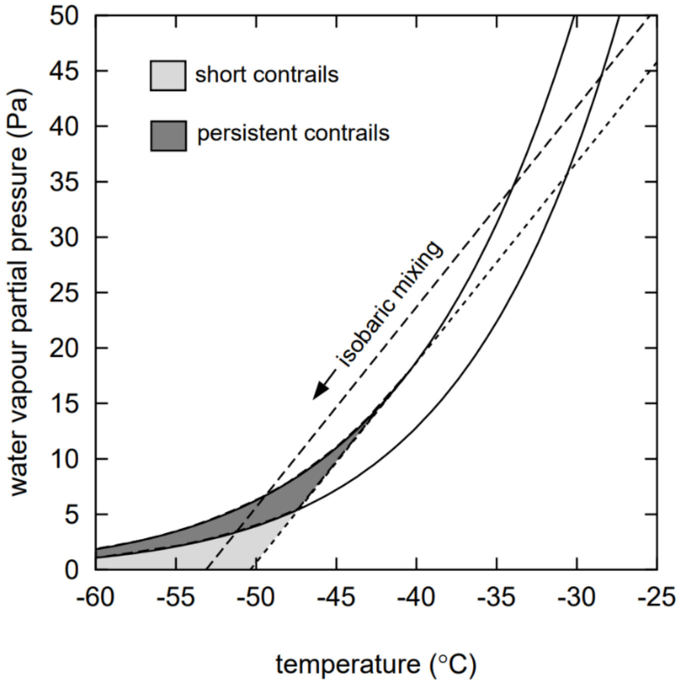

Figure 1: Mixing trajectories for two different exhaust plumes (dashed lines). The slopes of the mixing trajectories are given by G. The curves indicate the water vapor saturation partial pressure w.r.t. water (upper curve) and ice (lower curve). A parcel of air from one of the two exhaust plumes originates at the top right (outside of the plotted region) and, during the mixing with ambient air, travels along the mixing trajectory. Contrail formation occurs if the parcel becomes transiently (super-)saturated w.r.t. liquid water, i.e., if the mixing trajectory at least tangentially touches or intersects the upper curve. For contrails to persist, the ambient atmospheric conditions must lie in the darkly shaded grey region. In contrast, in the lightly shaded grey region, RH_{ice} < 100% and contrails will evaporate. Figure taken from Gierens, 2010.

2.3. Synoptic Meteorology and Ice Supersaturation

The synoptic scale describes meteorological processes that occur on typical length scales of several thousand kilometers (Wallace & Hobbs, 2006). On the synoptic scale, the mid-latitudes, the region of interest in this study, are characterized by the strong temperature gradient between polar and tropical air masses that gives rise to low-level cyclones, i.e., regions where the low-level atmospheric flow pattern is counter-clockwise (clockwise) in the Northern (Southern) hemisphere (Wallace & Hobbs, 2006).

These extratropical cyclones are characterized by baroclinicity, i.e., the density is not only a function of pressure (Martin, 2013). Consequently, in a baroclinic atmosphere, isotherms (lines of constant temperature) are not aligned with isobars (lines of constant pressure, Martin, 2013). This has two main implications. Firstly, the surface temperature gradient gives rise to density gradients and air parcels will experience buoyant lifting along regions of sharp temperature gradients, so-called fronts, which are associated with clouds and precipitation (Holton & Hakim, 2012). Secondly, the geostrophic wind will have a vertical shear due to the temperature dependence of the thickness between isobar layers, which is referred to as the thermal wind relationship (Holton & Hakim, 2012). This results in jet streams, i.e., regions of high wind speeds aloft along which the low-level cyclones propagate along the so-called storm tracks between 30° and 60° latitude (Wallace & Hobbs, 2006).

Fronts can be broadly subdivided into three categories (Ahrens & Henson, 2022):

- Cold fronts, where the surface temperature after the passage of the front is lower than before. Generally, cold fronts have a steep slope (approx. 1:50), along which cold air masses vertically displace warm air, causing the formation of convective clouds and thunderstorms (Ahrens & Henson, 2022).
- Warm fronts, where the surface temperature increases with the passage of the front. Their slope is much shallower than that of a cold front (approx. 1:300) (Ahrens & Henson, 2022). Generally, warm fronts are associated with a stable atmosphere and gentle uplift that yields stratiform clouds, which form several hundreds of kilometers ahead of the front (Ahrens & Henson, 2022).
- Occlusions, where warm air is wedged above cold air masses at lower levels. Occluded fronts can either be dominated by the characteristics of a cold- or a

warm front, although warm-type occluded fronts are more common than cold-front occluded fronts (Ahrens & Henson, 2022).

Weather patterns associated with frontal systems do not always strictly follow these rules: For example, a cold front in a dry atmosphere can occur without any significant convective weather, while thunderstorms can be embedded in a warm front within a moist and warm atmosphere in the summer months (Ahrens & Henson, 2022).

Ice supersaturation in the upper troposphere is often associated with frontal systems of extratropical cyclones because lifting occurs along fronts, either rapidly through convective processes or more gently in layered stratiform clouds (Gierens et al., 2012). During the lifting of a moist air parcel, its relative humidity increases, which can ultimately yield supersaturation w.r.t. ice.

Ahead of warm fronts, as RH_i gradually increases over hours, in-situ formation of non-aviation induced cirrus does not take place immediately as soon as RH_i increases above 100%, but only when RH_i has reached values well above 100% when homogenous or heterogenous nucleation can take place (Gierens et al., 2012). This temporal delay gives rise to cloud-free ISSRs, in which persistent contrails can form.

3. Data

3.1. WAWFOR Data (Experimental Data Set Klima 1)

World Aviation Weather Forecast (WAWFOR) data is generated specifically for aviation users using the ICON NWP model and includes parameters relevant for flight operations, e.g., icing and turbulence data (DWD, 2025c). WAWFOR forecasts are generated four times daily, with output lead times in one-hour increments up to a maximum lead time of 48 h (36 h for turbulence data) with a horizontal resolution of 0.0625° x 0.0625° (i.e., each grid box has a meridional extent of approx. 7.0 km and a zonal extent of approx. 2.3 to 6.0 km, depending on the latitude) for the EU-forecasts (available for the region 23.5°W to 62.5°E and 29.5°N to 70.5°N, DWD, 2025) and 0.25° x 0.25° for the global forecast. In aviation, altitudes are given as flight levels, where one flight level is equal to 100 ft under ICAO standard atmospheric conditions (100 ft ≈ 30 m, e.g., flight level 100, FL100 = 10.000 ft). Vertically, WAWFOR data is available for every tenth flight level between 50 and 600 and additionally for FL675 (DWD, 2025c). In this study, only the EU-forecasts between flight levels 300 up to and including 400 are considered (pressure levels 300 to 187.5 hPa, see Table 1).

Table 1: Flight levels and the corresponding pressure levels used in this study.

FL	300	310	320	330	340	350	360	370	380	390	400
p (hPA)	300.9	287.4	274.5	262.0	250.0	238.4	227.3	216.6	206.5	196.8	187.5

For my research, I use one of six experimental data sets that was generated for the D-KULT ("Demonstrator Klima- und Umweltfreundlicher Lufttransport", demonstration of climate- and environmentally friendly air transport; Matthes et al., 2026) research project to investigate the climate impact of aviation, Klima 1. The Klima 1 dataset is based on the output of the routine deterministic and ensemble ICON runs and was used for real-time experiments and archived for hindcasting simulations as part of the D-KULT project and has the same spatial and temporal resolution and the forecast time as the EU-forecast of the WAWFOR data set. The two parameters used in this study from the Klima 1 data set are:

- Potential Persistent Contrail (PPC): a binary value that indicates whether persistent can contrails form in the deterministic run.

- Probability of persistent contrails (PPC_{prob}): PPC averaged over the 40 routine ensemble runs of the ICON model. The PPC_{prob} field was originally calculated on a different grid and then interpolated onto the WAWFOR grid. Therefore, the values of PPC_{prob} are not discrete probabilities in 1/40 increments but have slightly different values between 0 and 1.

The PPC field is calculated using the temperature and humidity from the WAWFOR forecast in two steps. First, the Schmidt-Appleman-criterion is evaluated in each grid box assuming a propulsion efficiency of 0.365. Then, each grid box is evaluated for ice supersaturation (where the relative humidity w.r.t. ice is calculated using the relative humidity and the temperature from the WAWFOR fields). Because of a low-humidity bias in the forecast, the saturation threshold for RH_{ice} was lowered to 93% (Gierens et al., 2022; Hofer et al., 2024). PPC is 1 where SAC is fulfilled, and ice-supersaturation is present.

The deterministic run is the experiment from which operational weather forecasts are derived. The ensemble experiments, on the other hand, are used to quantify the internal variability of the climate system and to account for the fact that the initial state of the atmosphere is not perfectly known (Reinert et al., 2020). They are performed on a grid with a coarser resolution than the deterministic experiment and with slightly perturbated initial conditions (Reinert et al., 2020).

The WAWFOR Klima-1 datasets were retrieved from a tape archive as GRIB2-files and then converted into NetCDF-files. In total, the PPC and PPC_{prob} timeseries contain 348 days from February 2nd, 2024, until January 31st, 2025. This time frame was chosen to cover an entire year. Single days are missing because of issues in the retrieval process or because they were not readable. To analyze the evolution of the forecast, I use the 12:00 h forecast with a lead time of 01:00 h (12:00 h + 01:00 h) and the 00:00 h forecast with a lead time of 13:00 h (00:00 + 13:00 h).

3.2. Icon NWP Output

For the investigation of the synoptic situations on selected days where the forecast of PPC and PPC_{prob} was classified as especially robust or non-robust, results from the ICON numerical weather prediction NWP forecast were used. For these 20 days, only the 12:00 h forecast with a lead time of 01:00 h was considered. The variables investigated are the temperature (T), vertical velocity (OMEGA) and the relative humidity (RELHUM). The data is available for the 200, 250 and 300 hPa pressure levels and has the same spatial resolution as the PPC and PPC_{prob} fields (i.e., 0.0625° x 0.0625°). The NWP results were retrieved as NetCDF-data from the PAMORE system (DWD, 2025b).

3.3. ERA5 Reanalysis Data

For the calculation of backward trajectories, ERA5-reanalysis data (Hersbach et al., 2023) was used. Reanalysis data comprises results from model data and observations that are assimilated after the relevant date stamp. Unlike weather forecasts, the objective of reanalysis data is not to forecast the future state of the atmosphere but rather to provide a best estimate of the atmosphere at a given time in the past. ERA5 data is available for the period from 1940 onwards, on a 0.25° x 0.25° grid.

In this study, only the 250 hPa pressure level is considered. The main advantage of using ERA5 data instead of ICON forecast data is that they are easier to access and that more variables are directly accessible. For the calculation of backwards trajectories and their analysis, the horizontal wind components (u and v) the vertical velocity in pressure coordinates (W) the specific humidity (q) and the relative humidity (rh) were used. In ERA5 relative humidity is given w.r.t. ice if the temperature of the grid cells is below -23° C (Wolf et al., 2025). The ERA5 data was retrieved in the NetCDF format from the CDS climate data portal for the periods of June through August 2024 and November 2024 through January 2025 (Copernicus Climate Change Service, 2025).

3.4. Meteorological Data

WxFUSION's cb-global data provides nowcasting data of convective systems to aviation users based on satellite images from the METEOSAT 11's high resolution visible (HRV) channel (WxFUSION, 2023). Specifically, areas where rapid cloud growth occurs are identified and their movement analyzed and can be viewed by pilots and dispatchers in near real-time to avoid thunderstorms.

The surface analysis charts from the German Meteorological Service (DWD) are provided twice per day, at 00:00 h UTC and at 12:00 h UTC. They show isobars (lines of equal surface pressure), manually drawn fronts (cold fronts in blue with semi-circles, warm fronts in red with triangles, and occlusions in purple) and are useful in gaining an overview of the meteorological situation on the synoptic scale (DWD, 2025a). The 00:00 h UTC surface analyses were retrieved for 20 selected days and used to identify fronts in the proximity of ISSRs for the selected robust and non-robust days.

4. Research Methods

4.1. Conditional Distribution of PPC_{prob} where PPC = 1

As a measure for how well the ensembles' forecasts agrees with the deterministic forecast, first PPC_{prob} (i.e., the average PPC of all ensemble members) under the condition that PPC = 1 in the deterministic run was analyzed. This distribution (probability density function) is denoted as $f(PPC_{prob} \mid PPC = 1)$.

To test for statistical significance between the seasonal distributions and other distributions that were analyzed in this thesis, a two-sample Kolmogorov-Smirnov-Test was used. The null hypothesis of this test is that two samples with sizes m and n originate from the same distribution. For large samples, it can be rejected at the significance level α under the condition that

$$D_{m,n} > c(\alpha)\sqrt{\frac{n+m}{nm}}$$

where $c(\alpha = 0.01) = 1.628$ and $D_{m,n}$ is the KS-statistic given by the maximum distance between the cumulative distribution functions (CDFs) of the samples.

One of the goals of this research project is to answer whether there are synoptic situations, under which the forecast of ISSRs is particularly robust or not. To answer these questions, twenty days were selected for further analysis by ranking them according to the median of the distribution $f(PPC_{prob} \mid PPC = 1)$. The underlying assumption for this approach is that a day with a low (high) agreement between PPC and PPC_{prob} indicates a non-robust (robust) forecast, in the sense that the 40 ensemble members agree poorly (well) with the deterministic model run. These days are not necessarily the days with the 'best' or 'worst' forecast (as evaluating the quality of the forecast would require the comparison of the forecast with observational data, which is not done in this study) but are merely used to measure the uncertainty of the model by comparing the results of the ensemble runs with the deterministic run.

4.2. Mean Contrail Length

A key metric to characterize contrail statistics is the mean contrail length (MCL), which is the mean length of the contrails formed by aircraft passing through a given region. To calculate the MCL, the PPC field for every timestep and every pressure level is sliced along every 25th latitude band and the length of all grid cells where PPC = 1 along this latitude band is summed. Finally, to obtain the mean contrail length, the total length where PPC = 1 along the latitude band is divided by the number of occurrences where PPC transitions from 0 to 1 in W-E-direction. The latitude increment of 25 grid boxes is chosen to reduce autocorrelation between the resulting contrail lengths, as the distance between 25 grid boxes corresponds to approx. 150 km, which is the average length of a contrail (e.g., Gierens & Spichtinger, 2000; Spichtinger & Leschner, 2016). An intuitive way to think about this approach is that the slices along one band of latitude represent flight paths of fictitious aircraft passing through the model grid from West to East. The MCL represents the mean length of the contrails resulting from the flights on these fictitious West-East trajectories.

The size of grid boxes is given by a constant latitude and longitude increment of 0.0625° in either direction. Since the distance of one degree longitudinal difference depends on the latitude, the length of a grid box in W-E direction, dx, is given by the following formula:

$$dx = 0.0625 * \cos(\phi) * 1852\, m * 60$$

where φ is the latitude of the grid box.

4.3. Receiver Operating Characteristics

One of the challenges of comparing PPC and PPC_{prob} is that the former takes on a binary value while the latter is a probability with values between 0 and 1. To address this issue, an approach outlined by Hanst et al. (2025) is followed to convert the ensemble forecasts into a binary value, using a threshold value, k, to investigate where the PPC and PPC_{prob} values differ from one another spatially. All grid boxes where PPC_{prob} is above (below) k, are considered to have a PPC value of 1 (0). The 'constructed' PPC value from the ensembles shall be denoted PPC_{ens}:

$$PPC_{ens} = \begin{cases} 0 \text{ where } PPC_{prob} < k \\ 1 \text{ where } PPC_{prob} \geq k \end{cases}$$

This yields four possible cases for the relationship between PPC_{ens} and PPC, which are listed in Table 2.

Table 2: Contingency table for PPC_{ens} and PPC.

	PPC_{ens} = 1 (PPC_{prob} > k)	**PPC_{ens} = 0 (PPC_{prob} < k)**
PPC = 1	True positive (TP)	False negative (FN)
PPC = 0	False positive (FP)	True negative (TN)

From these cases, two important metrics, the probability of detection (POD) and the false prediction rate (FPR), can be derived. The POD is defined as the proportion of all grid cells where PPC = 1 that is correctly identified by the ensemble prediction system, i.e., PPC_{prob} > k:

$$POD = \frac{TP}{TP + FN} = \frac{n[(PPC_{prob} > k) \cap (PPC = 1)]}{n(PPC = 1)}$$

where n(…) denotes the number of grid cells that fulfill the condition given in brackets.

The FPR is a measure for the proportion of all grid cells where PPC = 0 where the ensemble prediction system falsely predicts a PPC_{prob} > k, although PPC = 0:

$$FPR = \frac{FP}{TN + FP} = \frac{n[(PPC_{prob} > k) \cap (PPC = 0)]}{n(PPC = 0)}$$

Both POD and FPR depend on the chosen value for k. For a higher k, both the POD and FPR will be lower. An ideal forecast would have a POD = 1 and an FPR = 0, meaning that the forecast would not miss any events while simultaneously predicting no false positives. Since no forecast is perfect, the challenge remains in finding a value for k that minimizes both the costs incurred due to false positives and missed predictions. To quantify this trade-off and to find an optimum value for k that yields a high POD and a low FPR, the Youden Index can be defined:

$$Youden\ Index = POD - FPR$$

The Youden Index was calculated for different values of k between 0 and 1 in 0.1 increments.

4.4. Autocorrelation Scales of Selected Meteorological Properties

To characterize the synoptic situations on the robust and non-robust days, the autocorrelation lengths of selected parameters that play a role in the formation of ISSRs (temperature, vertical velocity and relative humidity) were calculated from the ICON NWP data on the robust and non-robust days (Hofer et al., 2024). The T-, W- and RH-fields were reduced in dimension to include only every 25th latitudinal band from the ICON NWP, which gives a total of 27 latitude bands per pressure level. Next, the horizontal autocorrelation function along each latitudinal band was calculated.

Autocorrelation is the correlation of a dataset with a lagged version of itself and can be used to identify recurring patterns in timeseries or spatial data. It can take values between -1 and 1. Per definition, the autocorrelation has a value of 1 for a lag of 0 and decreases with increasing lag and eventually reaches values close to 0, where it cannot be interpreted as a signal but rather as noise instead. The lag at which the autocorrelation drops below a certain value is the autocorrelation scale and can be considered as a characteristic horizontal length for processes.

4.5. Treatment of Meteorological Variables

4.5.1. Vertical Moisture Flux

Fluxes are calculated by multiplying a density with velocity. Since both the ERA5 and ICON output is in pressure coordinates, the units of the vertical velocity, w, is Pa s^{-1}, which can be interpreted as the pressure change that a parcel experiences (Holton & Hakim, 2012). Lifting motions correspond to a decrease of pressure (w < 0), while descending motions correspond to an increase in pressure (w > 0). From the vertical velocity and the specific humidity, the vertical moisture flux was calculated at each time step by converting the vertical velocity into cartesian coordinates (Holton & Hakim, 2012) and multiplying it with the specific humidity:

$$F_{moist,v} = -\frac{\omega * q}{g}$$

where g = 9.81 m s^{-2}. This gives the vertical vapor flux in kg m^{-2} s^{-1}. The daily vertical moisture transport in kg m^{-2} was calculated by adding up the vertical moisture flux at each time step over 24 hours and multiplying by 3,600 s. Notably, due to the conversion from natural coordinates into cartesian coordinates, the sign of upward motion differs between ω (in uplift conditions, ω < 0) and the vertical moisture flux (in uplift conditions, $F_{moist,v} > 0$).

4.5.2. PPC from ERA5 reanalysis Data

Since the ERA5 data does not include parameter PPC, PPC for the ERA5 data, PPC_{ERA}, had to be evaluated derived from T and RH, by assessing whether the SAC was fulfilled, and ice supersaturation was present. To check if the SAC was fulfilled, the critical temperature, T_C, was calculated using a formula after Schumann (1996):

$$T_C = -46.46 + 9.43 \ln(G - 0.053) + 0.720[\ln(G - 0.053)]^2$$

where G denotes the slope of the saturation vapor pressure curve.

If both conditions, i.e., $T < T_C$ and RH > 93%, are fulfilled, $PPC_{ERA} = 1$.

4.5.3. Normalized Geopotential Height

For the display in upper-level meteorological charts, the geopotential height from the ICON operational weather forecasts was normalized, following an approach outlined by Wilhelm et al., (2022). This has the advantage that the geopotential takes on values between approx. 0.9 and 1.1, independent of the pressure level, which enables a direct comparison between different pressure levels.

For the normalization, first a characteristic scale height $\overline{H} = \frac{R_d \overline{T}}{g} = 7{,}452\ m$ was calculated using the gas constant for dry air and assuming a constant gravitational acceleration and a constant atmospheric temperature of 255 K. The normalized geopotential height was then calculated using the following formula:

$$Z^*(p) = \overline{H} \ln\left(\frac{p_s}{p}\right)$$

where a standard surface pressure of 1,000 hPa was assumed for p_s. This gives standard geopotential heights of 8,972 m, 10,331 m, and 11,994 m for the 300 hPa, 250 hPa and 200 hPa pressure levels, respectively.

4.5.4. Temperature Lapse Rate

The temperature lapse rate was calculated from the ICON operational forecast data by taking the temperature at the 200 hPa and 300 hPa pressure levels, using the following formula:

$$\gamma = \frac{g}{R_d} \frac{\ln(T_0/T_1)}{\ln(p_0/p_1)}$$

where p_0 and T_0 (p_1 and T_1) denote the temperature and pressure at 200 hPa (300 hPa; Wilhelm et al., 2022).

4.6. Lagrangian Trajectories

The Lagrangian trajectories were calculated from ERA5 reanalysis data. To select the starting points, only values where $PPC_{ERA} = 1$ at the initial time of the forecast for the ten robust and non-robust days were selected over a regularly spaced 2° x 2° longitude-latitude grid that was placed over the model domain.

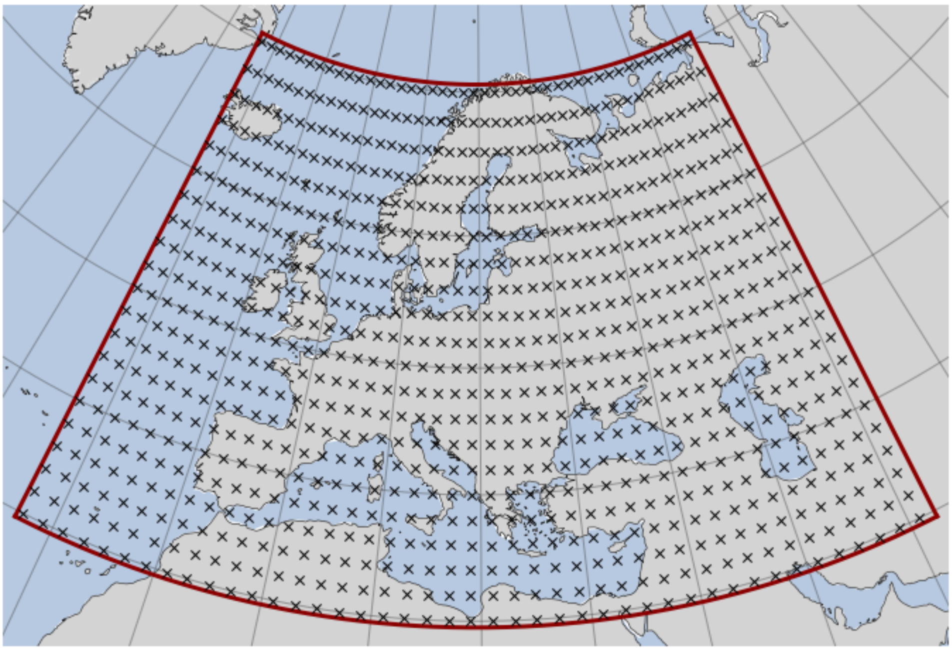

Figure 2: Region considered in this study (i.e., the ICON EU model domain, marked by the red outline) with all possible starting points for the Lagrangian backwards trajectories, denoted by the "x" markers. The starting points for the trajectories were chosen from the locations where PPC = 1.

A first-order Eulerian iteration scheme (Brannan et al., 2015) was used to calculate the latitude and longitude of the air parcels at t_{i-1} (where lat_i denotes the latitude of the air parcel at t_i):

$$lon_{i-1} = lon_i - \frac{u(t_i, lon_i, lat_i) * \Delta t}{(60 * 1852 \frac{m}{\circ}) * \cos(lat_i)}$$

and

$$lat_{i-1} = lat_i - \frac{v(t_i, lon_i, lat_i) * \Delta t}{(60 * 1852) \frac{m}{\circ}}$$

with Δt = 3600 s, the time step of the ERA5 reanalysis data. Because the resulting longitude and latitude values lie between the grid cells, the relevant meteorological parameters as well as the u- and v-components of the wind field required for the calculation of the next pair of coordinates were obtained by taking the values from the nearest grid cell.

Due to computational constraints, the backwards trajectories were only calculated on the 250 hPa pressure level, i.e., vertical movement across different pressure levels was suppressed. The backwards trajectories were calculated for 24 time steps, i.e., until 13:00 h UTC on the preceding day. For each trajectory, the specific humidity q, the relative humidity RH, the temperature, the horizontal wind speed ($\sqrt{u^2 + v^2}$) and the vertical velocity in pressure coordinates (ω) were saved at each time step.

5. Results

5.1. Conditional Distribution of PPC_{prob} where PPC = 1

The time series of the median f(PPC_{prob} | PPC = 1) displays a seasonal pattern with a minimum in the late spring and early summer months and a maximum in the winter months (the seasons are defined as follows: winter: December to February, DJF; spring: March to May, MAM; summer: June to August, JJA; fall: September to November, SON; see Figure 3). Compared with the forecast at 00:00 h with a lead time of 13 hours, the forecast with a lead time of only one hour at 12:00 h shows a better agreement between the deterministic forecast and the ensemble forecasts, i.e., f(PPC_{prob} | PPC = 1) concentrates more to its maximum value of one (i.e., the median is closer to one). This can be ascribed to small differences in the initial conditions of the individual ensembles, which propagate and grow over multiple time steps. This also explains the higher spread of the ensemble forecasts as seen in the higher standard deviation in the forecast with a longer lead time.

Additionally, the overall ice saturation (i.e., the proportion of all grid boxes where PPC = 1) also shows a seasonal cycle, with a higher share of grid cells with PPC = 1 occurring in the winter months and the lowest values of ice supersaturation occurring in the summer months.

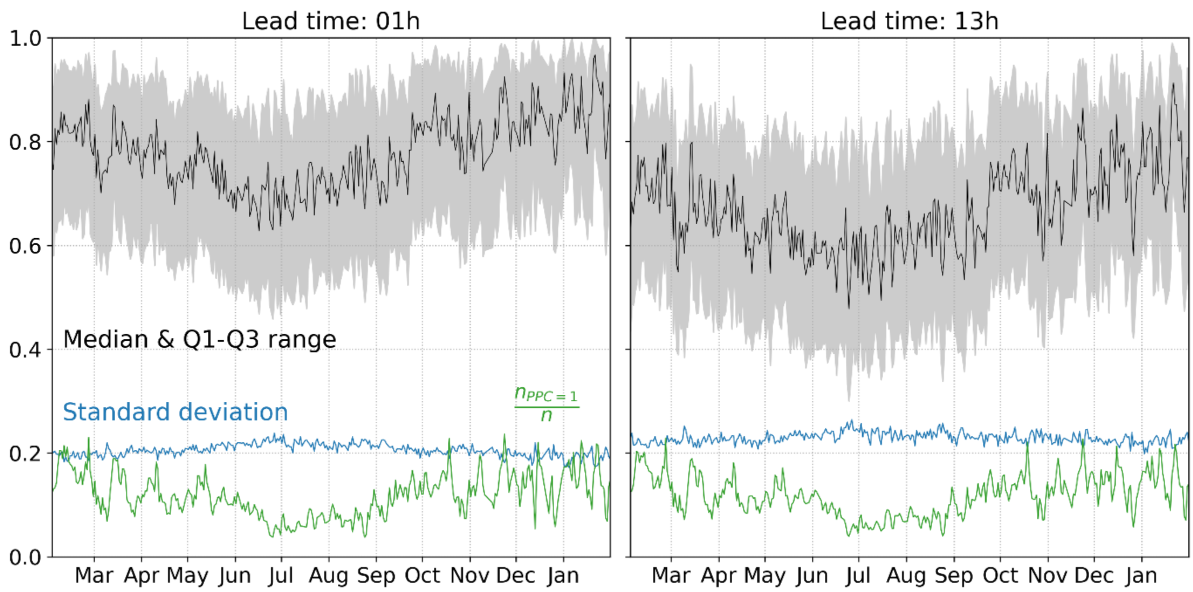

Figure 3: Daily median (black), Q1-Q3 range (shaded in grey), standard deviation (light blue) and the proportion of the conditional distribution f(PPC_{prob} | PPC = 1) and the proportion of all grid cells where PPC = 1 as a measure for the overall ice supersaturation ($n_{PPC=1}/n$, where n is the number of grid cells, green) for the 12:00 h forecast with a lead time of 01 h (left) and the 00:00 h forecast with a lead time of 13 h.

To further investigate the seasonality of f(PPC_{prob} | PPC = 1), the daily timeseries were regrouped into seasonal datasets. To test for statistical significance, the data had to be reduced in size first due to computational constraints. This size reduction was performed by selecting only every 25th grid box in x- and y-direction which additionally has the advantage of mitigating potential effects of autocorrelation. Then, using a two sample KS-test, each seasonal pairing (e.g., DJF vs. JJA) was found to be statistically significant at the 0.01 significance level.

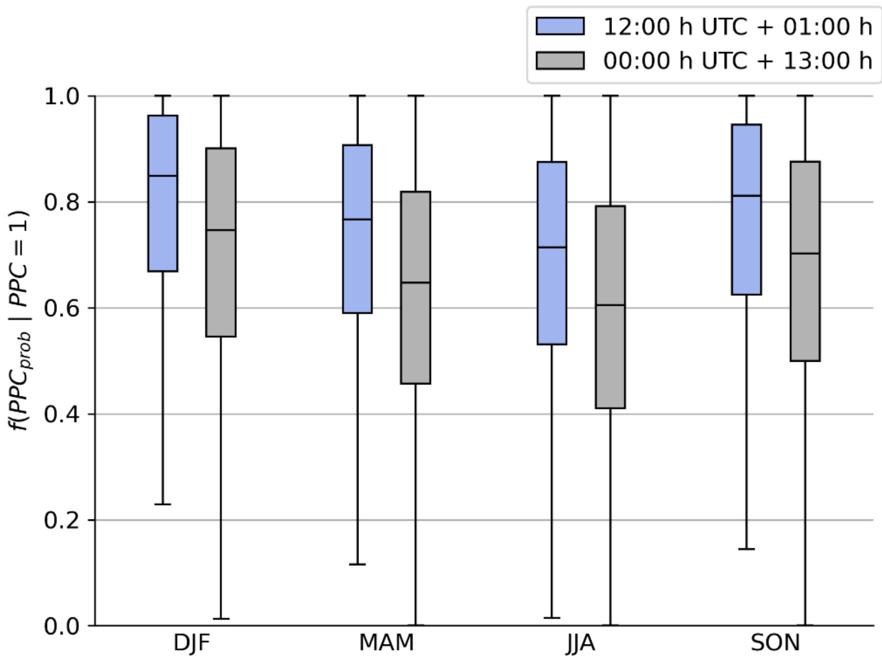

Figure 4: Boxplot of the conditional distribution PPC_{prob} | PPC = 1 for the four different seasons for the 12:00 + 01:00h forecast (blue) and the 00:00 + 13:00h forecast (green). The box indicates the range between the first and third quartile, the horizontal blue and green lines in the boxes represent the median and the whiskers indicate the 1.5 interquartile range (IQR). Outliers are not shown.

Finally, for the selection of the robust and non-robust days, the ten days with the lowest and highest median were chosen from the conditional distribution f(PPC_{prob} | PPC = 1). These days were chosen so that subsequent days are avoided (to reduce temporal autocorrelation in the dataset) and so that they are among the best or worst for forecasts with both lead times. The subsets are:

- Robust days:
  - November 2024: 20th, 23rd
  - December 2024: 15th
  - January 2025: 1st, 4th, 06th, 12th, 20th, 22nd, 26th

- Non-robust days:
    - June 2024: 1st, 10th, 16th, 23rd, 30th
    - July 2024: 3rd, 7th, 17th, 22nd
    - August 2024: 24th

As expected from the seasonal cycle in the forecasts, the values with the highest median values occur in the fall and winter months, whereas the values with the lowest median values occur in the summer months.

5.2. Mean Contrail Length

The annual cycle of the MCL and the MCL for each pressure level are shown in Figure 5. The MCL over all levels and timesteps is 152 km for the 12:00 + 01:00h forecast, which agrees well with a study using airborne-measured relative humidity (Gierens & Spichtinger, 2000). Additionally, the MCL shows a strong positive Pearson r-correlation with the median PPC_{prob} under the condition that PPC = 1 ($r = 0.8714$, $p < 0.01$). Although the MCL is lower for the 00:00 + 13:00 h forecast with a value of 116 km, both the Pearson correlation between MCL and median f(PPC_{prob} | PPC = 1) show the same pattern, which is why only the results for the 12:00 + 01:00 h are presented in this section.

For the 12:00 + 01:00 h forecast, the MCL has a minimum at the 300.9 hPa pressure level (FL300) of around 137 km and increases to a maximum of 162 km at 196.8 hPa (FL390) before dropping slightly at 187.5 hPa (FL400). The Pearson correlation coefficient has a maximum at the 300.9 hPa level (FL300) and decreases with increasing altitude. Finally, the MCL for the sets of the ten robust (non-robust) days is 280 km (90 km), suggesting that the uncertainty in the forecasts of regions where persistent contrails occur could be closely linked with the horizontal extent of regions where contrails occur.

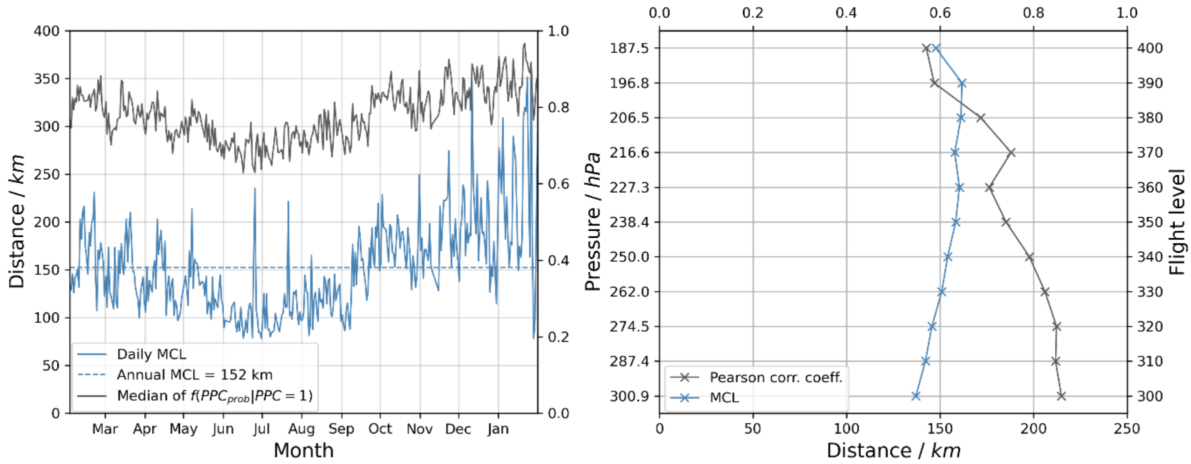

Figure 5: Daily MCL and median f(PPC_{prob} | PPC = 1) (left). MCL calculated over the entire timeseries and the Pearson correlation coefficient between MCL and the median f(PPCprob | PPC = 1) for each pressure level (right). The results are displayed for the 12:00 + 01:00 h forecast.

5.3. Receiver Operating Characteristics

The receiver operating characteristics (ROC) curve displays the probability of detection (POD) against the false prediction rate (FPR) for different threshold values, k. A high agreement between PPC_{prob} and PPC fields is indicated by the proximity of the curve to the upper left corner (where the FPR = 0 and the POD = 1). As expected, the ROC curve for the forecast with a lead time of 1 hour is closer to this target than the forecast with a lead time of 13 hours. The Youden Index is highest for a value of k = 0.3, which is chosen as a threshold value for the plots of PPC_{prob} and PPC (see Figure 6).

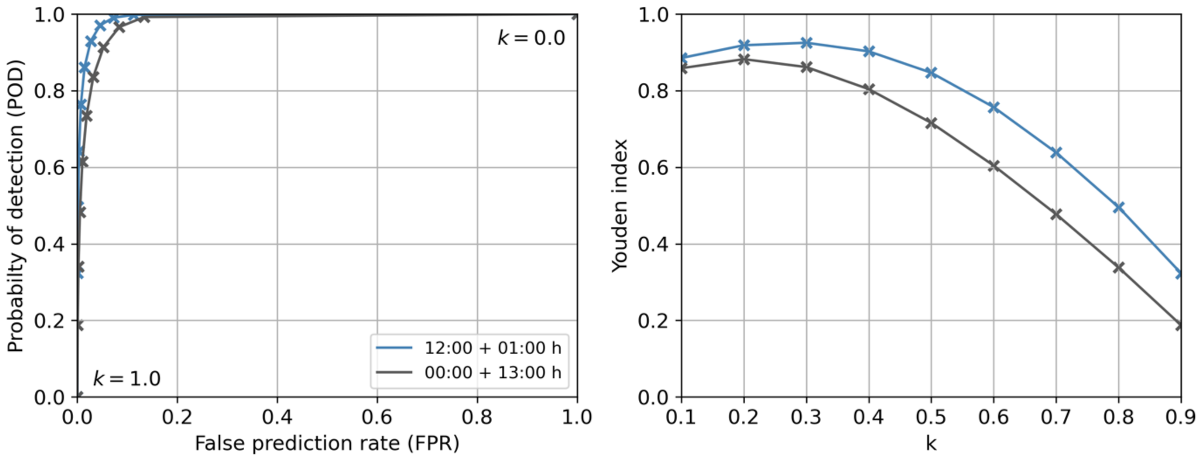

Figure 6: ROC curve for the 12:00 + 00:01 h and 00:00 + 13:00 h forecast (left) for different values of k ∊ {0.0, 0.1, 0.2, …, 1.0} and the Youden Index (right).

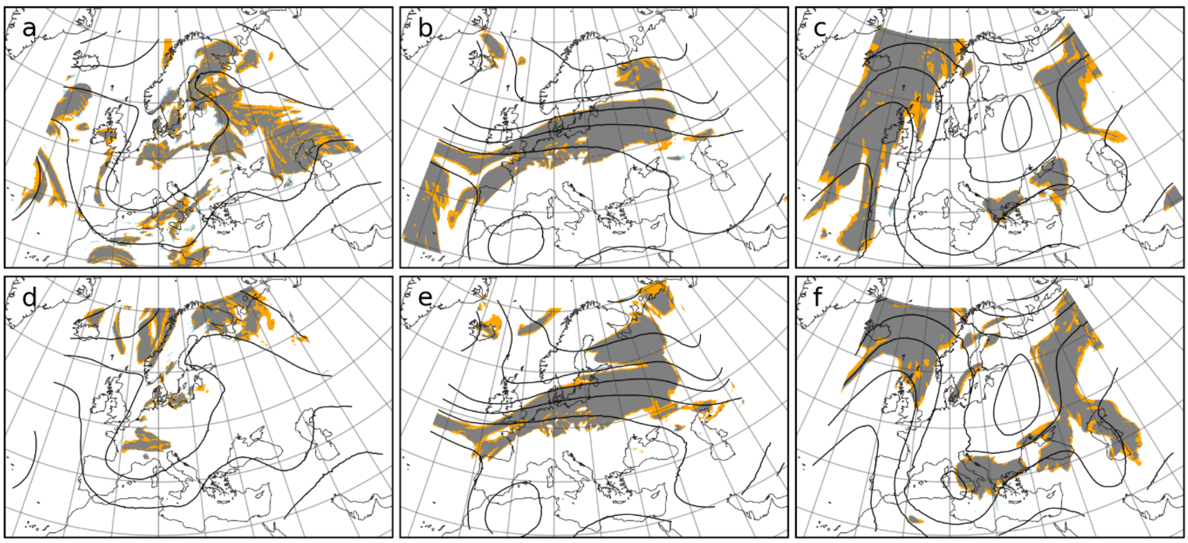

Figure 7: PPC and PPCprob fields on June 01st, 2024, one of the non-robust days for FL340 (250 hPa, a) and FL300 (300.9 hPa, d), on January 01st, 2025 (p = 250 hPa, b, p = 300.9 hPa, e), one of the robust days with a zonal pattern, and on January 12th, 2025 (p = 250 hPa, c, p = 300.9 hPa, f), one of the robust days with a blocking pattern. Grey areas indicate true positives (PPC = 1 and PPC_{prob} > 0.3), orange areas indicate false positives (PPC = 0 and PPC_{prob} > 0.3) and light blue areas indicate false negatives (PPC = 1 and PPC_{prob} < 0.3). The solid black lines indicate the normalized geopotential.

Both the robust and non-robust days show only a low number of false negatives. This can be attributed to the low value of k of 0.3 that was chosen for the threshold value, which means that for the pseudo-deterministic value PPC_{ens} to be 1, only 3 out of 10 ensembles need to have a PPC value of 1.

January 12th, 2025 (one of the days from the subset robust days), is characterized by few relatively large regions where the PPC = 1 in the Western part of the model grid, upstream of a strong upper-level ridge associated with high wind speeds a strongly curved flow. The other robust day shown in Figure 7, January 01st, 2025. is characterized by a strong zonal flow along which an elongated ISSR extends from the Eastern North Atlantic, over the North and Baltic Seas and into North-Eastern Europe. On both robust days, the uncertainties (i.e., the FPs and the few FNs) occur at the edges of the ISSRs. This was observed on all the robust days.

In contrast to this, the regions where PPC = 1 are more diffuse, overall smaller and spread out over the entire model domain on June 1st, 2024. Uncertainties are not only observed near the edges but also in the center of some ISSRs. These findings agree with the analysis of the MCL and indicate a link between the horizontal scale of ISSRs and the robustness of the ISSR forecasts.

5.4. Autocorrelation of Vertical Velocities

The autocorrelation scales for the vertical velocity (OMEGA), relative humidity (RELHUM) and temperature (T) for the robust and non-robust days are displayed in figures Figure 8 and Figure 9. While there are no distinct differences between the robust and the non-robust days in the autocorrelation of the relative humidity and temperature fields, the autocorrelation lengths for the vertical velocity differ from one another notably. The autocorrelation level was defined to be 0.25, as for values below this threshold, the signal becomes noisy for the vertical velocity fields.

For the subset robust (non-robust) days, the median autocorrelation lengths of the vertical velocity are 58, 104 and 80 km (26, 34 and 35 km) for the pressure levels 200, 250 and 300 hPa, respectively. Using a two-sample KS-test, this difference between the distributions was found to be statistically significant at the 0.01 significance level (see also the cumulative distribution function in Figure 10).

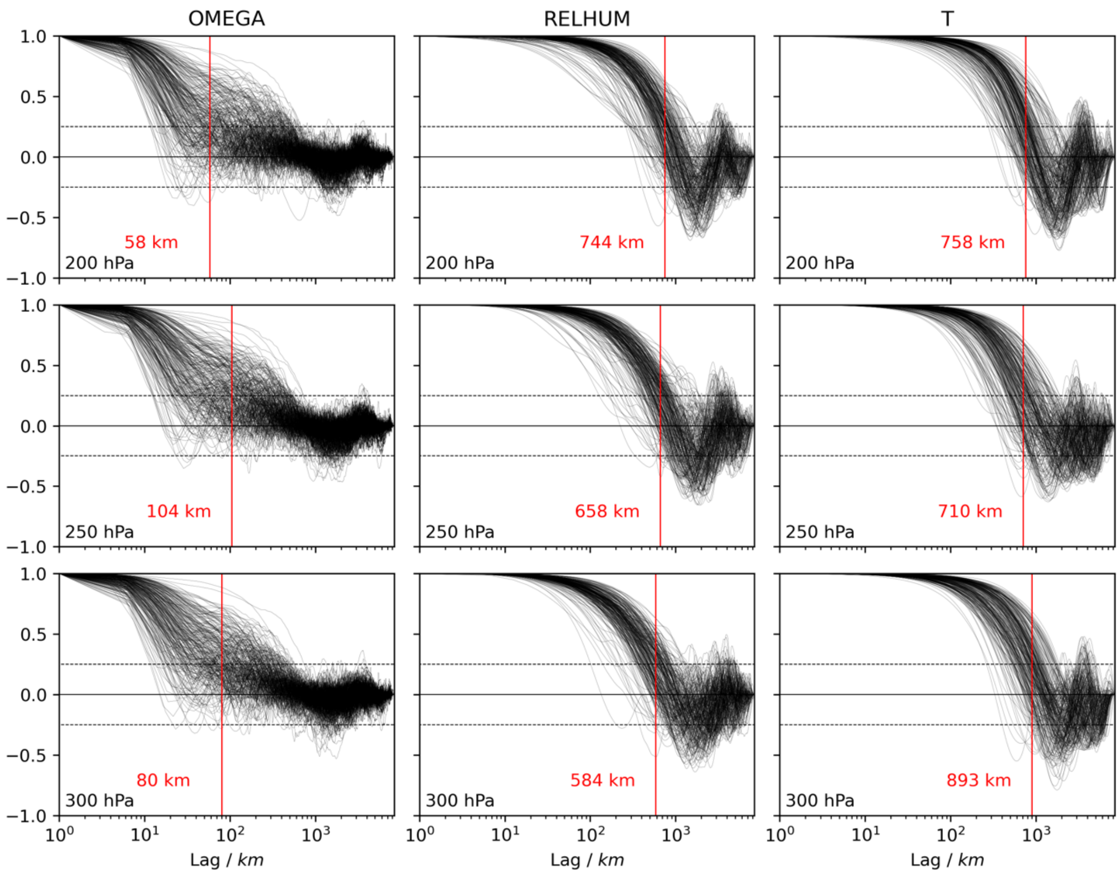

Figure 8: Autocorrelation length of the vertical velocity (OMEGA), relative humidity (RELHUM) and temperature fields for the 12:00 + 01:00 h forecast from the PAMORE dataset for the 200, 250 and 300 hPa pressure levels (FL390, FL340 and FL300, respectively) for the robust days. The median of the respective distribution is indicated by the red line. In each subplot, ten days of 27 latitude bands are plotted, giving a total of 270 lines per plot.

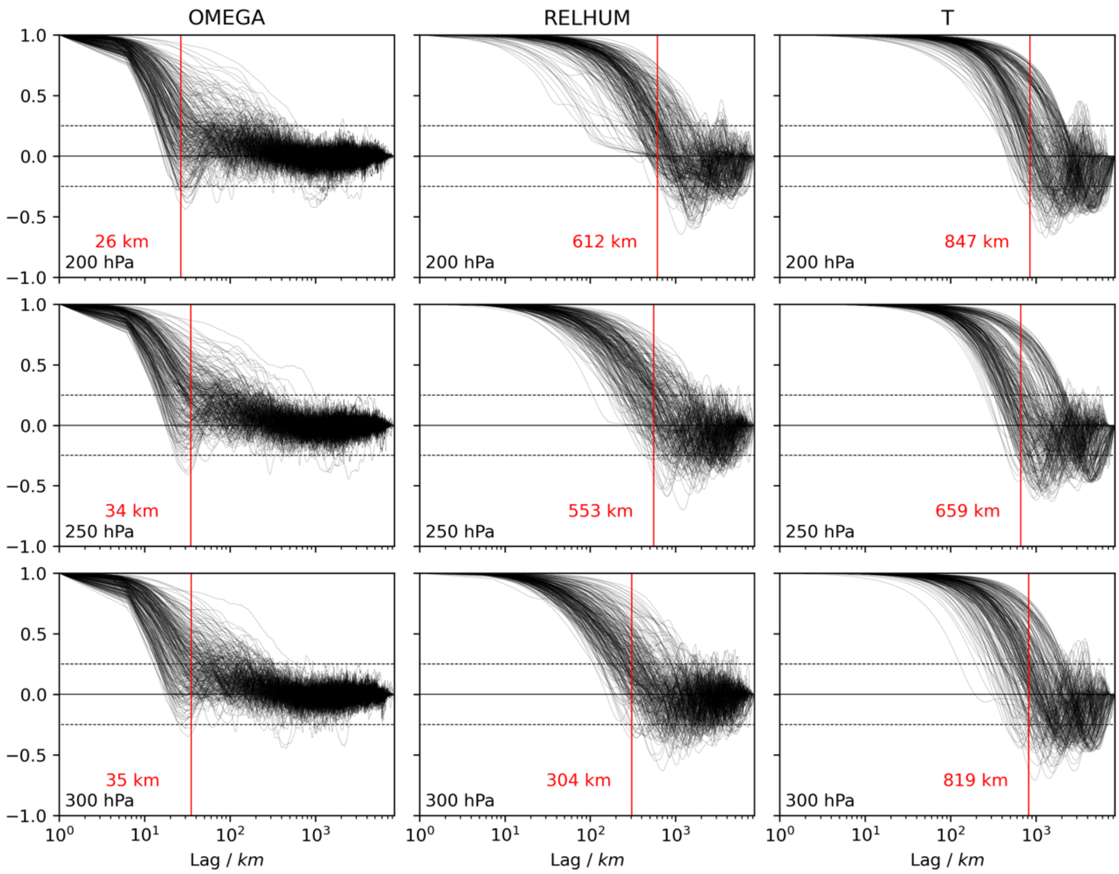

Figure 9: As for Figure 8 but for the non-robust days.

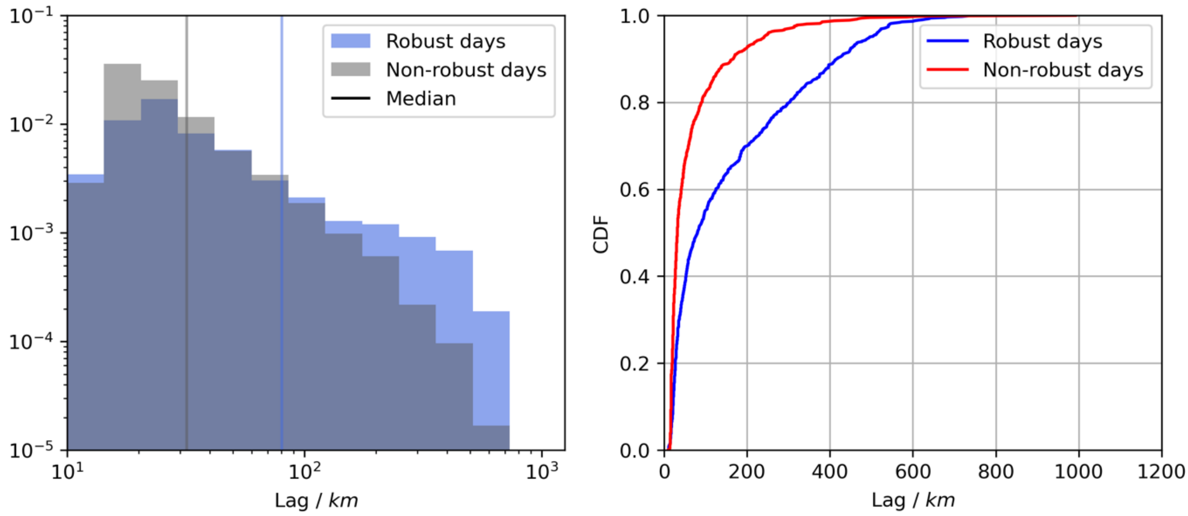

Figure 10: Histogram of the distribution of the autocorrelation scale of the vertical velocity for the robust and non-robust days in a log-log plot and the cumulative distribution function for both distributions (CDF, right).

5.5. Synoptic Situation on the Selected Days

The upper troposphere on days with a robust forecast are characterized by strong and clearly-defined geopotential consistent with frontal systems. ISSRs are large spread and often extend over at least five of the considered pressure levels (approx. 50 hPa, or 1,500 m vertically). Even though both blocking and zonal patterns occur in the subset of the robust days (see Figure 11) there is not one "typical" synoptic situation that can be used to describe the subset of the robust days. In contrast, on the non-robust days, the geopotential gradients in the upper troposphere are weaker. ISSRs are overall smaller, more isolated and rarely extend over five or more of the considered pressure levels.

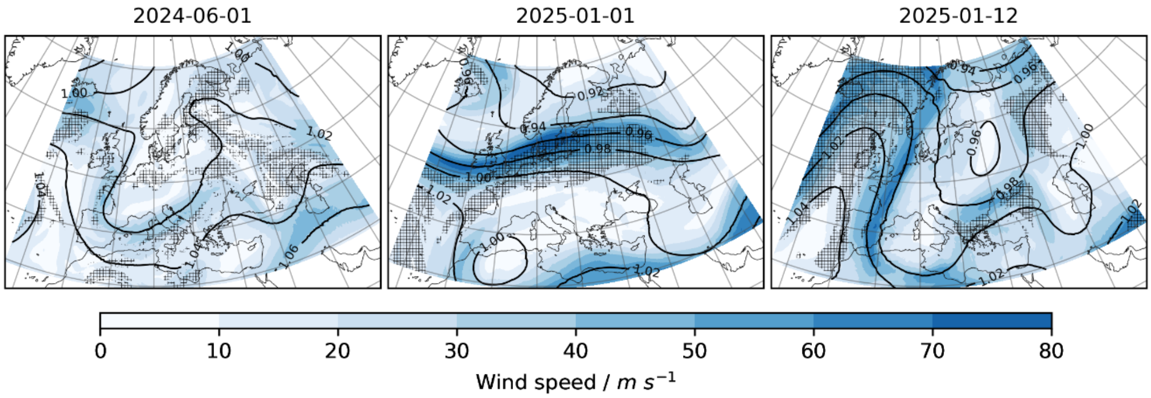

Figure 11: Synoptic situation at p = 250 hPa on June 01st, 2024 (left) as an example for one of the non-robust days, January 01st, 2025 (center), one of the robust days with a zonal pattern and January 12th, 2025 (right), one of the robust days with a blocking pattern. The shaded regions indicate areas where PPC=1, the solid lines are lines of equal normalized geopotential.

On both robust and non-robust days, regions where PPC = 1 are characterized by a weak lifting motion, which is more pronounced on the robust days (mean value -0.065 Pa s^{-1} at p = 250 hPa) compared with the non-robust days (mean value -0.053 Pa s^{-1} at p = 250 hPa). Additionally, the horizontal wind speeds on the robust days are stronger (mean value 35.4 m s^{-1} at p = 250 hPa) than on the non-robust days (mean value 20.7 m s^{-1} at p = 250 hPa).

Distributions for lapse rates on the robust and non-robust days within and outside of ISSRs are shown in Figure 12. Regions where ISSRs occur are associated with higher lapse rates on the robust days (median lapse rate 6.95 K km^{-1} in regions where PPC = 1 vs. 2.82 K km^{-1} in regions where PPC = 0). In other words, the atmosphere is characterized by a much weaker stability within PPC = 1 regions, compared with PPC = 0 regions. On the non-robust days, even though the distributions of the lapse rates significantly differ from one another (using a two-sample KS-test, α = 0.01), the median lapse rate within ISSRs is only slightly higher (4.84 K km^{-1}) than outside of ISSRs (4.62 K km^{-1}). These results are consistent with a previous study by Wilhelm et al. (2022). Notably, lapse rates within ISSRs are much higher on the robust days than on the non-robust days.

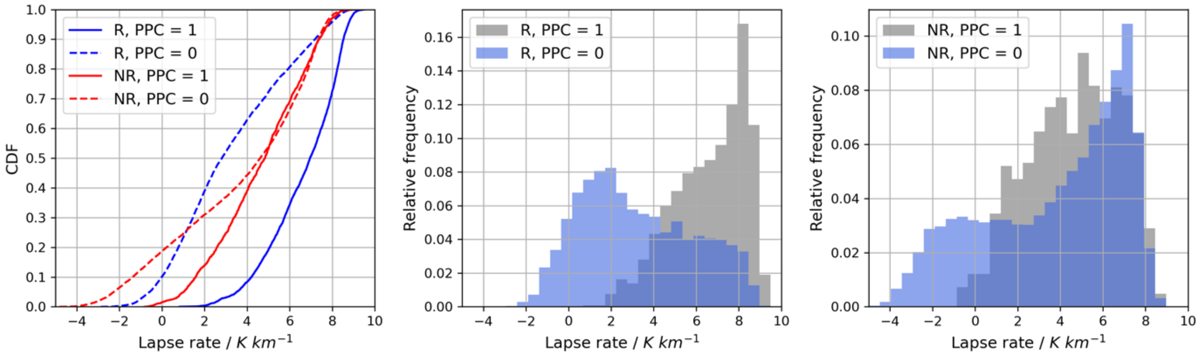

Figure 12: Cumulative distributions of lapse rates on robust (R) and non-robust (NR) days (left) for regions where PPC = 1 and regions where PPC = 0, and histograms of the lapse rate distributions on robust (center) and non-robust days (right), both for regions where PPC = 1 and PPC = 0.

5.6. Lagrangian Trajectories

Sample trajectories for three of the robust and non-robust days each, are shown in Figure 13 with the PPC_{ERA} = 1 regions. Additionally, the vertical moisture flux, integrated over the 24 hours prior to 13:00 h UTC on the respective robust or non-robust day is shown. At first glance, it is already obvious that the trajectories on the non-robust days pass through regions with an enhanced integrated vertical moisture transport.

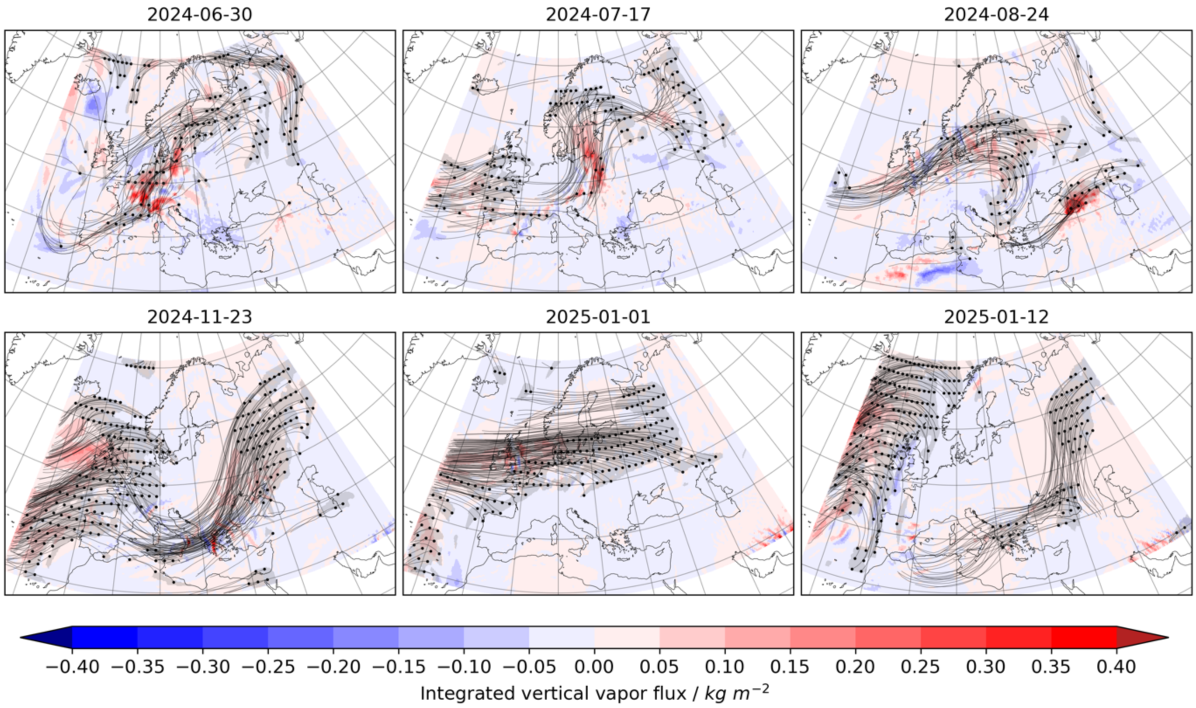

Figure 13: Sample trajectories for three robust days (upper three plots) and three non-robust days (lower three plots). The black lines indicate the individual trajectories. Grey shaded regions indicate the ERA5 PPC = 1 regions, derived from ERA5 temperature and relative humidity on the relevant day at 13:00 h UTC. The blue and red regions denote the integrated vertical moisture flux in the 24 hours prior to 13:00 h UTC on the relevant day.

Estimating the mean length of the trajectories does not make sense in this experiment, as a considerable proportion of the trajectories extend beyond the limited model domain. To investigate the average horizontal trajectory movement, a more meaningful property is the average horizontal wind speed, V_h. The mean, median and standard deviation for selected properties of the Lagrangian trajectories are presented in Table 3. The air parcels experience more lifting on average on the robust days than on the non-robust days and, on average stronger wind speeds. The standard deviation of vertical velocity differs only slightly between the robust and non-robust days. These findings are consistent with the results from the ICON forecast in the ISSRs at the forecast time 13:00 h UTC.

Table 3: Statistical properties of selected properties of the Lagrangian trajectories for the robust (R) and non-robust (NR) days.

	w (Pa s^{-1})		V_h (m s^{-1})	
	R	**NR**	**R**	**NR**
Mean	-0.077	-0.048	31.8	22.4
Median	-0.063	-0.031	28.8	20.3
STD	0.156	0.145	15.1	12.2

Figure 14 depicts histograms for the distributions of the relative humidity w.r.t ice, vertical velocity and vertical moisture flux for all points in the trajectory in the subset of the robust and non-robust days. For each variable, the distributions were found to significantly differ from one another at the α = 0.01 significance level using a two-sample KS-test. The relative humidity distributions for both robust and non-robust days indicate that a substantial amount of the air parcels were not supersaturated over the entire period of the 24 hours. Additionally, the relative frequency of the relative humidity distributions displays a strong peak at RH = 100%, which is more pronounced on the robust days than on the non-robust days. The distributions of the vertical moisture flux display a larger spread on the non-robust days (standard deviation 1.97 x 10^{-6} kg m^{-2} s^{-1}) than on the robust days (standard deviation 7.74 x 10^{-7} kg m^{-2} s^{-1}) and have slightly positive median values (robust days 1.42 x 10^{-7} kg m^{-2} s^{-1}; non-robust days: 2.26 x 10^{-7} kg m^{-2} s^{-1}).

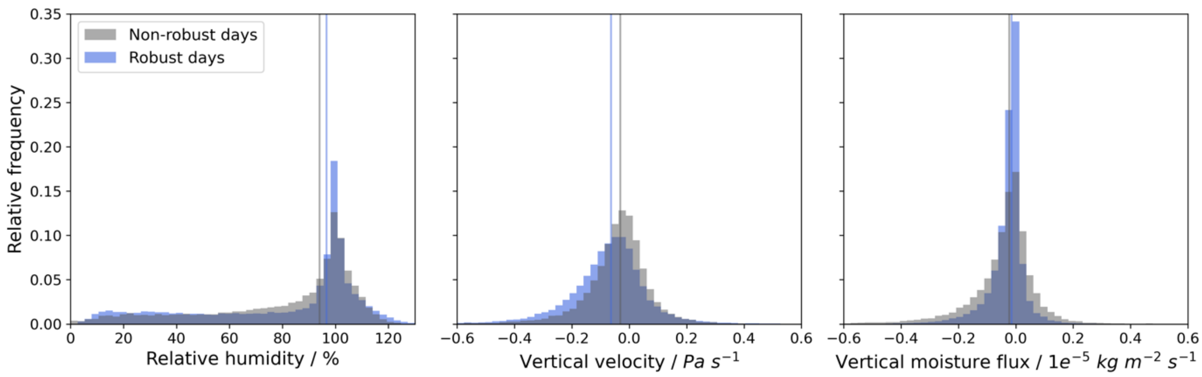

Figure 14: Histograms of the relative humidity (left), vertical velocity (center) and vertical moisture flux (right) of all trajectories calculated on the non-robust days (grey) and on the robust days (light blue). The vertical lines indicate the median of the respective dataset. The histograms for all six distributions were calculated with n = 50 bins.

The median temperature, relative and specific humidity of all trajectories at each time step are displayed in Figure 15. The air parcels experience a cooling and increases in both relative and specific humidity on both the robust and non-robust days. Notably, the median temperature of air parcels on the robust days is about 8 °C colder on the robust days than on the non-robust days. Despite only small differences in the median relative humidity, the median specific humidity is approx. 0.06-0.07 g kg^{-1} lower on the robust days than on the non-robust days. This can be attributed to the saturation vapor pressure's exponential dependance on temperature.

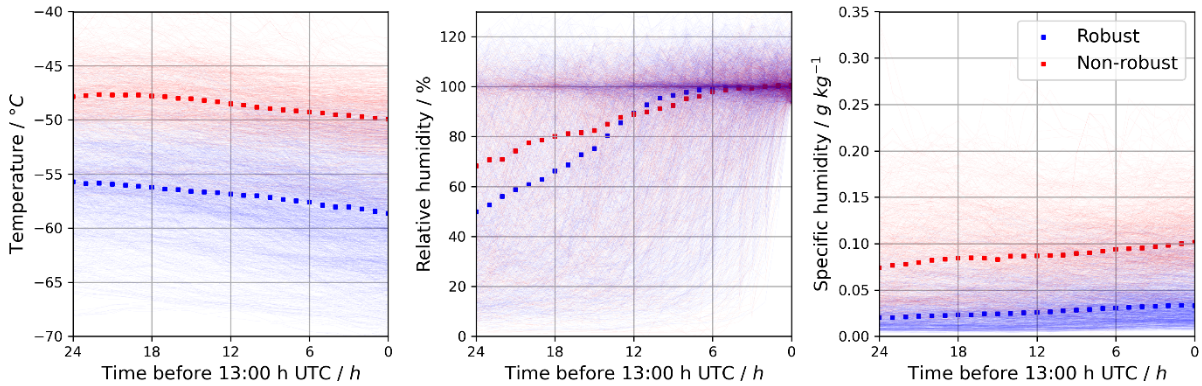

Figure 15: Evolution of temperature (left), relative humidity (center) and specific humidity (right) in the trajectories over the 24 hours prior to the 13:00 h UTC on the robust (blue) or non-robust (red) days. The very thin red and blue lines are the values for each trajectory, while the blue and red boxes indicate the median of all trajectories in the subset robust or non-robust days. The median values of the temperature, relative and specific humidity shown here differ from the median values of the difference that the individual air parcels experience. This is because not all trajectories have the same length. If an air parcel is outside of the model boundary at that time step, it is not considered in this plot. For instance, a trajectory with a temperature decrease of 3 °C over 24 hours will have a much shallower slope than a trajectory with the same temperature decrease over only six hours.

Besides the median at each timestep, the differences for each trajectory were calculated by taking the difference in the respective parameter of the first time step (always 13:00 h UTC on the selected day) and the last time step of that trajectory. Since a high number of the trajectories also extended beyond the model domain where no data is available, not all trajectories reach the maximum possible length of 25 time steps.

Generally, the air parcels from the ISSRs experience a cooling, which is more pronounced on the robust days (median -3.00 °C) than on the non-robust days (-1.45 °C) and an increase in relative humidity. At the same time, the temperature in ISSRs is lower on the robust days (mean -56.8 °C) than on the non-robust days (mean -47.1 °C). However, despite the increase in relative humidity, the air parcels' specific humidity remains nearly constant on the robust days (median 0.21 x 10^{-3} g kg^{-1}) but shows an increase on the non-robust days (median 9.02 x 10^{-3} g kg^{-1}). The distributions were found to be statistically significant on the 0.01 significance level using a two-sample KS-test. This indicates that on the non-robust days, saturation is mainly driven by mixing between air parcels, whereas on the non-robust day, cooling mainly drives the RH_i increases.

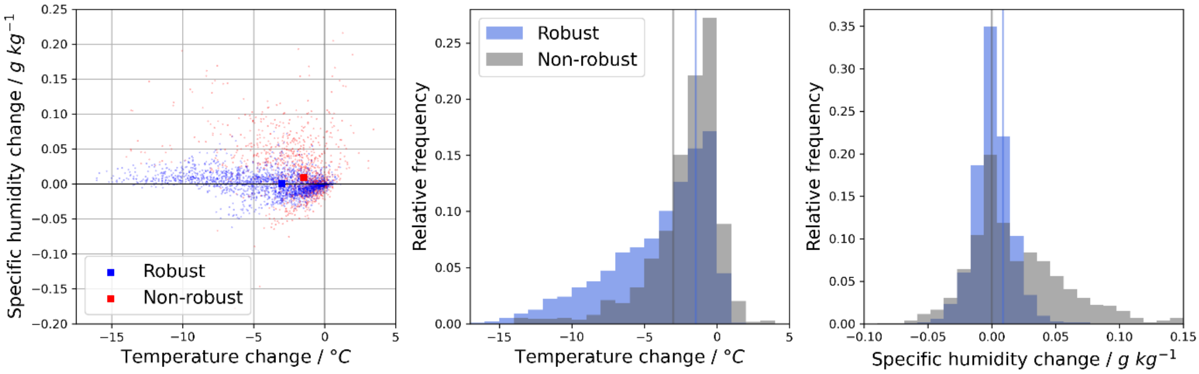

Figure 16: Scatterplot of all the temperature and specific humidity changes of all trajectories on the robust (blue) and non-robust days (red, left), where the squared markers indicate the median of both subset and histograms for the temperature (center) and specific humidity changes (right) for both subset of days (robust blue, non-robust grey).

6. Discussion

6.1. Criterion for the Choice of the Robust and Non-robust Days

The sole criterion for the selection of the robust and non-robust days is the median $f(PPC_{prob} \mid PPC = 1)$. The advantages of using the conditions PPC = 1 is that PPC is a binary value, while PPC_{prob} can take on continuous values between 0 and 1. This approach is therefore mathematically simple and easy to implement.

In the majority of the ISSRs that were considered in this study, PPC_{prob} is one (or close to one) near the center and drops towards the edges of the PPC = 1 region. This implies that in smaller ISSRs the edges will have a larger influence on the median $f(PPC_{prob} \mid PPC = 1)$ than in larger ISSRs. The seasonality in the median $f(PPC_{prob} \mid PPC = 1)$ reflects this geometric effect: Smaller ISSRs in the summer months are associated with a lower median $f(PPC_{prob} \mid PPC = 1)$, while larger ISSRs in the winter months generally have a higher median $f(PPC_{prob} \mid PPC = 1)$.

The analysis of the synoptic situations on the robust and non-robust days, both by means of the backward Lagrangian trajectories and the analysis of the ICON NWP data, confirm that the dynamics of the upper troposphere on the robust and non-robust days differ significantly. It therefore appears that the smaller, more frayed ISSRs in the summer and the larger, more coherent ISSRs in the winter, are a consequence of underlying dynamics that give rise to different formation mechanisms. In other words, it is exactly the small ISSRs in the summer months that the NWP struggles to predict.

One possible caveat of the approach of only considering the median $f(PPC_{prob} \mid PPC = 1)$ as a proxy for the robustness of the forecast is that regions where PPC = 0 are neglected. To address this issue, the threshold-based approach outlined in section 4.3 was used to investigate the uncertainty ratio, which I defined as the ratio of the area where the ensemble forecast and the deterministic forecast do not agree (i.e., the sum of FP and FN) to the areas where both the ensemble and the deterministic forecasts both indicate PPC = 1 (i.e., TP):

$$Uncertainty\ ratio = \frac{FP + FN}{TP}$$

For example, an uncertainty ratio of 0.5 for an individual ISSR implies that 50% outside of the robust regions (where ensemble and deterministic forecasts agree, i.e., PPC = 1 and $PPC_{prob} > k$) will be non-robust (i.e., the results of the deterministic forecast and the ensemble forecasts disagree). The uncertainty ratio has two advantages over the median f(PPC_{prob} | PPC = 1). Firstly, it considers the area where non-robust forecasts occur in relation to the ISSR. Secondly, regions where PPC = 0 are considered by including the false positives.

The uncertainty ratio exhibits a seasonal, but opposite pattern as the median f(PPC_{prob} | PPC = 1), with the highest uncertainty occurring in the summer months and the lowest values in the winter months (see Figure 17). On the robust (non-robust days), median f(PPC_{prob} | PPC = 1) highs (lows) and uncertainty ratio lows (highs) coincide, which confirms that the median f(PPC_{prob} | PPC = 1) is a sound choice as a proxy for the selection of the robust and non-robust days.

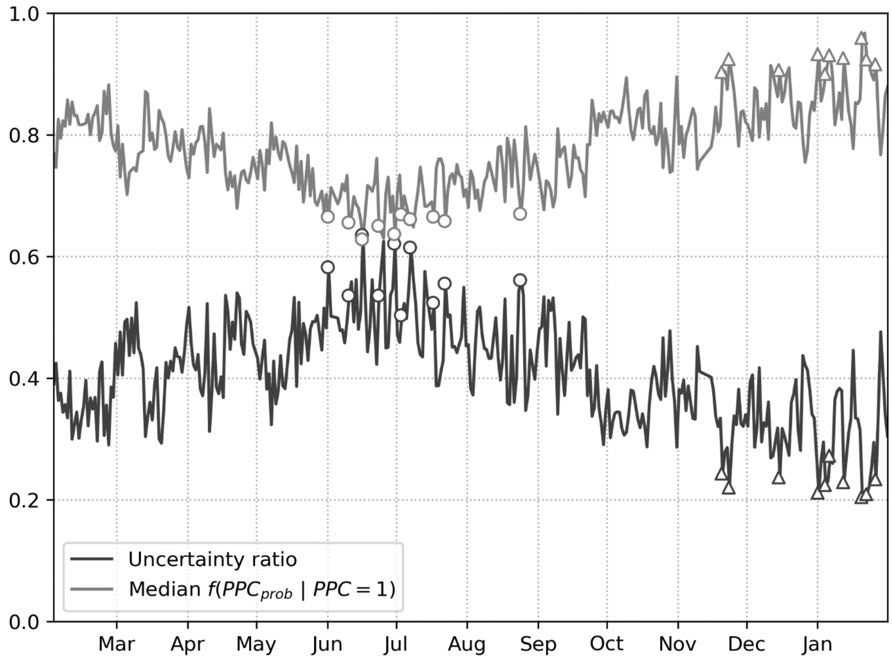

Figure 17: The annual cycle of the uncertainty ration ((FP+FN)/TP) and the median f(PPC_{prob} | PPC = 1). The triangles (circles) indicate the respective values on the robust (non-robust days).

Finally, it should be considered that the deterministic forecast and the ensemble prediction serve two different purposes: While the deterministic forecast is generally used as the operational weather forecast and is calculated on a finer grid, the purpose of the ensemble prediction is to measure the model’s uncertainty by running the weather forecast multiple times with slightly different initial values to account for natural variability and uncertainty in the initial conditions (Reinert et al., 2020). Therefore, the ensemble mean PPC_{prob} does not automatically make the ensemble forecast more meaningful from a physical point of view but should be considered as a metric that measures the spread between the ensembles.

6.2. Synoptic Situation on the Selected Days

Generally, ISSRs on the robust days occur in regions with an anticyclonic flow, high wind speeds and often span hundreds or thousands of kilometers. The atmosphere on these days is characterized by strong geopotential height gradients, which indicates an overall high degree of organization. In contrast, on the non-robust days, the atmosphere is more chaotic, which is reflected in smaller geopotential height gradients and weaker horizontal winds. ISSRs are more fragmented and smaller in dimension, as shown in the significantly shorter mean contrail lengths. Additionally, the smaller autocorrelation scales of vertical velocity on the non-robust days compared with the robust days reveal that atmospheric processes occur on a smaller scale. The backward Lagrangian trajectories also confirm that air parcels transition more often between super- and subsaturation on the non-robust days than on the robust days, before finally reaching PPC = 1 towards the end of a trajectory. On both the robust and non-robust days, a substantial amount of the ISSRs at the 250 hPa pressure level could be linked to frontal systems in the DWD surface analysis. However, while on the robust days surface fronts are mainly associated with strong pressure gradients at the surface that, despite moving horizontally, persist over multiple days, the surface fronts are not as persistent on the summer days.

These results are consistent with a recent study by Schuh et al. (2025), who found a seasonal pattern in the fractal dimensions of ISSRs, with lower values in the summer time (indicating more frayed ISSRs) and higher values in the winter (indicating ISSRs with a more elongated shape). The authors conclude that the reason for the seasonality of the ISSRs' fractal dimension is due to different formation mechanisms, i.e., large-scale frontal lifting in the winter months and deep convective activity in the summer months.

The backwards trajectories reveal that on the robust days, ice supersaturation is mainly driven by cooling. This is consistent with a case study by Spichtinger et al. (2005) who used backwards trajectory modeling to show that in a warm conveyor belt (a region of enhanced moisture flux associated with a frontal zone), supersaturation was mainly driven by cooling. This effect is exacerbated by the overall lower temperatures in the ISSRs on the robust days: due to the exponential nature of the Clausius-Clapeyron equation, the saturation vapor pressure (and thus also the relative humidity) is more sensitive to temperature changes at lower temperatures. For instance, a cooling of

-3.00 °C towards a final temperature of -56.8 °C, the average temperature of an ISSR at 250 hPa on the robust days, results in a change in saturation vapor pressure w.r.t. ice from 2.44 Pa to 1.66 Pa, a relative difference of -32.0%.

On the other hand, a cooling of -1.45 °C towards a final temperature of -47.1 °C, the average of ISSRs at 250 hPa on the non-robust days, corresponds to a change in saturation vapor pressure w.r.t. ice from 6.67 Pa to 5.61 Pa, a relative difference of only -15.9%. Therefore, the cooling in the summer months is likely not sufficient to increase relative humidity towards ice supersaturation but additional moisture must be added to the air mass. Indeed, on the non-robust days, the air parcels are subjected to less cooling but an overall stronger increase in specific humidity, which indicates mixing as the main driver for ice supersaturation on the non-robust days.

In comparison to the strong horizontal flow driven by geopotential gradients on the robust days, the non-robust days are characterized by non-linear scale interactions associated with convective activity combined with weaker horizontal winds. This causes disturbances to grow quicker in the summer than in the winter months, which likely poses a challenge for NWP models (Schumann & Seifert, 2025).

6.3. Vertical Velocity Field on the Selected Days

The vertical velocity field is of particular interest in the context of ice supersaturation in upper levels because lifting processes play a key role in the formation of ISSRs (Gierens et al., 2012). The median vertical velocity within ISSRs (derived at the time of observation from the ICON forecast results) and in the air parcels over 24 hours prior to the forecast (derived from the Lagrangian backward trajectories) is lower, which indicates more uplift, on the robust days than on the non-robust days. This might seem to contradict the hypothesis that deep convective activity is the driving factor for the formation of ISSRs in the summer as this is generally linked to strong updrafts and higher vertical velocities (Wallace & Hobbs, 2006). However, since deep convection in the summer months is isolated and typically occurs on a much smaller spatial scales than frontal lifting, it is not surprising that strong lifting cannot be identified from the median (or mean) of the vertical velocities (Wallace & Hobbs, 2006). Rather, the stronger lifting that occurs in ISSRs on the robust days is an indicator that ISSRs form in active lifting regions along frontal systems, where large-scale lifting is expected to occur in the vicinity of ice supersaturation. This finding is further supported by the substantially higher lapse rate associated with ISSRs on robust days. Generally, high lapse rates are associated with less atmospheric stability (Gierens et al., 2022). The weaker average lifting in ISSRs on the non-robust days in the summer, coupled with weaker lapse rates indicate that ISSRs do not coincide with dynamically unstable regions and active lifting. However, lifting could have taken place at some time in the past.

One of the robust days (22.07.2024) could be identified as a day with thunderstorms (personal exchange with Dr. Arnold Tafferner). To estimate the magnitude of the vertical velocities associated with deep convection in the ERA5-data and ICON forecast data, a satellite image was compared with the vertical velocity from ERA5 reanalysis and ICON forecast data at 250 hPa. The satellite image shows large thunderstorms over central Italy, Austria and the Czech Republic, and along the Balkan coast and smaller, more isolated thunderstorms further East over Belarus, Romania, and Bulgaria. While the larger thunderstorms clusters can be linked to regions where the minimum velocity reach values more than -1 Pa/s, the smaller thunderstorms cannot be clearly identified merely from the vertical velocity fields. Within the considered region (-10°W to 30°E and 35°N to 62.5°N), the absolute vertical velocity minimum is -1.52 Pa/s (approx. 0.5

m s^{-1} in height-based coordinates) in the ERA5 reanalysis and -2.80 Pa/s (approx. 0.9 m s^{-1} in height-based coordinates) in the ICON forecast data. These values are significantly less than observed up- and downdrafts in thunderstorms that can reach values of tens of meters per second (Wallace & Hobbs, 2006). This is most likely due to spatial averaging over an entire grid cell and temporal averaging over 1 h and the models' limitations in accurately representing sub-grid, turbulent processes. Additionally, the average thunderstorm lifetime of approx. 30 minutes is half of the ERA5 output time step (Wallace & Hobbs, 2006). The effect of spatial averaging already becomes apparent when comparing the ICON and ERA5 data: The minimum vertical velocities in the ICON model with a grid resolution of 0.0625° x 0.0625° are almost twice the minimum vertical velocities in the ERA5 model with a grid resolution of 0.25° x 0.25°. Notably, both models do not fully represent the convective processes that occurred in reality: the ICON model does not show any strong lifting processes in the Mediterranean region (Balkan coast and central Italy), while the ERA5 reanalysis data does not indicate strong lifting in the Baltic region (see Figure 18).

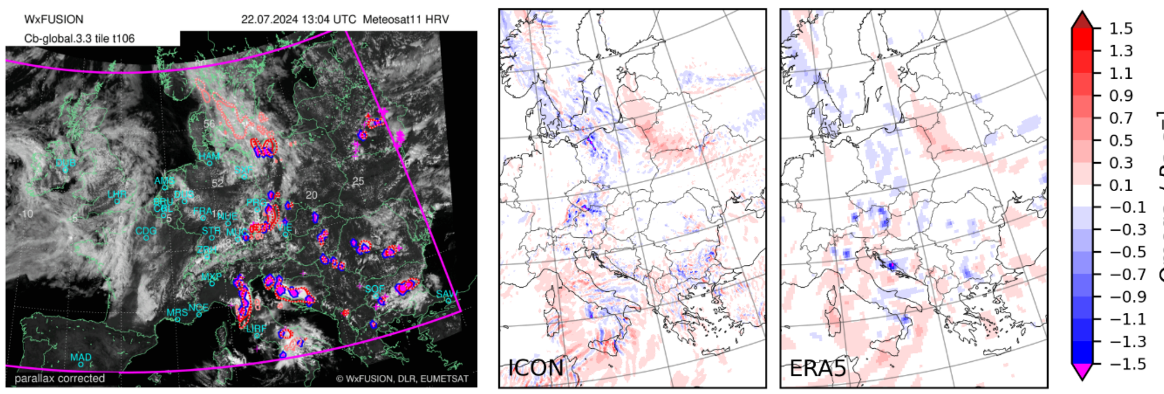

Figure 18: Satellite image (left) of the convective situations at 13:04 h UTC (the figure was kindly provided by WxFUSION GmbH), vertical velocities at p = 250 hPa from the ICON forecast data (12:00 h UTC + 01:00, center) and ERA5 reanalysis data (13:00, right) on 22.07.2024, one of the non-robust days. The magenta areas in the satellite image indicate active thunderstorms that were identified as they coincide with measured lightning activity and rapid cloud growth.

However, vertical velocity values exceeding 1 Pa s^{-1} are not always an indicator for the presence of deep convective activity. For example, on 12.01.2025, one of the robust days, the vertical velocity fields reach values of -2.08 Pa s^{-1} (ERA5) and even -5.69 Pa s^{-1} over Northern Norway (ICON, see Figure 19).

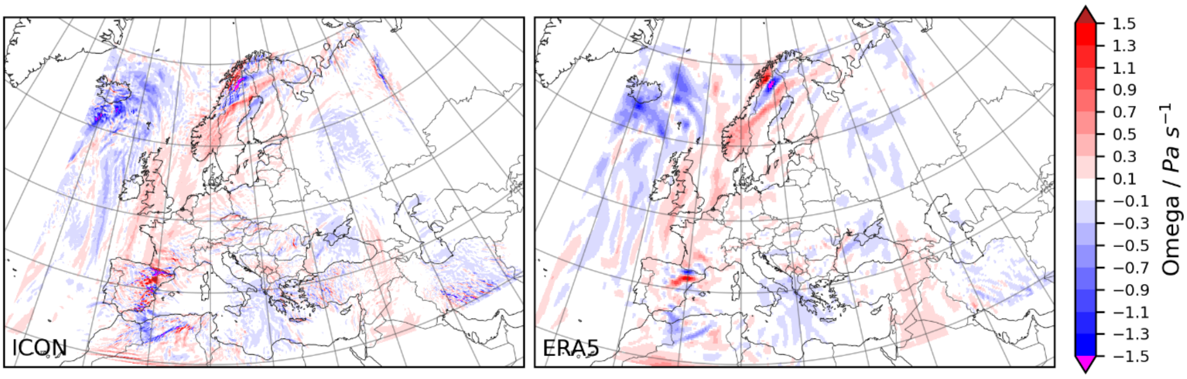

Figure 19: ERA5 (left) and ICON (right) vertical velocities at p = 250 hPa at 13:00 h UTC on 12.01.2025, one of the robust days.

The DWD surface analysis chart at 00:00 h UTC shows a strong low-pressure system over the Western North Atlantic and a strong high-pressure system over the English Channel. In the upper troposphere, this day is characterized by a strong jet stream, with horizontal wind speeds reaching up to approx. 75 m s^{-1} (see Figure 20).

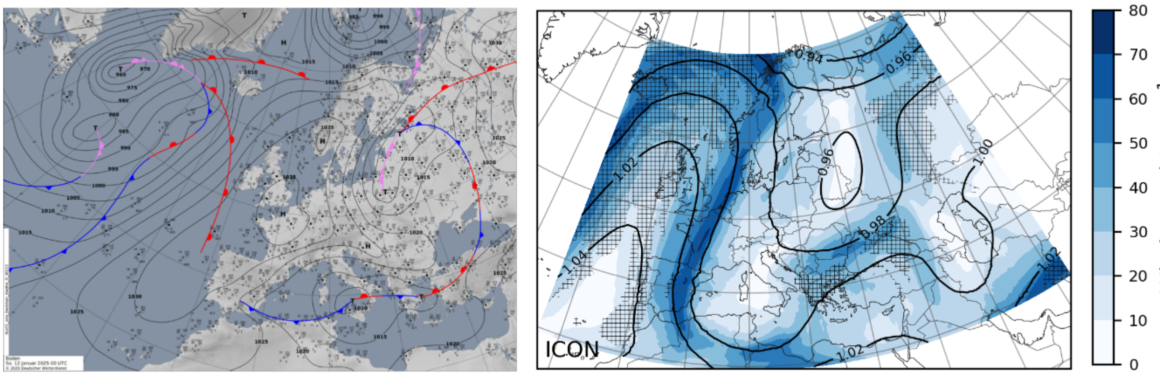

Figure 20: Surface analysis at 00:00 h UTC on 12.01.2025 of the DWD ((c) DWD, retrieved from Wetterzentrale.de (left, (c) DWD, 2025a, retrieved from Müller & Floors, 2026) and the wind speed and normalized geopotential height at p = 250 hPa for the 12:00 h UTC + 01:00 h forecast on 12.01.2025 (right). The stippled regions indicate PPC = 1.

Despite the strong updrafts over Norway on this day, there is little reason to believe that there was any deep convection on this day since the surface analysis does not indicate the presence of a front in the proximity. Additionally, during the winter, solar radiation is low and there is little energy available to foster convection. Instead, the strong winds aloft and the high surface pressure gradients suggest the uplift is rather caused by gravity waves over mountainous terrain on this date. Finally, a large ISSR can be found in the anticyclonic ridge, which coincides with a region of large-scale strong ($w < -1$ Pa s^{-1}) lifting. This is a good example for lifting along a warm conveyor belt, where warm, moist air ascends along a warm front. During their ascent, the relative humidity increases and eventually, ice supersaturation occurs (Spichtinger et al., 2005).

The vertical velocity from the Lagrangian backwards trajectories indicate that strong uplift (< -1 Pa s^{-1}) occurs along 0.11% of all trajectories on the robust days (43 out of 38,797 data points) and along 0.26% of all trajectories on the non-robust days (63 out of 24,249 data points). Even though lifting is stronger on average in the trajectories on the robust days than on the non-robust days, strong lifting exceeding -1 Pa s^{-1} occurs more frequently on the non-robust than on the robust days.

In contrast to the small-scale thunderstorms that occur on the warm summer day, the large-scale ascent along the warm front occurs over a much larger portion of the model grid. On the robust days, frontal systems are associated with high pressure gradients and stronger wind speeds. These are likely less sensitive to perturbations of the initial conditions and therefore ISSRs associated with frontal systems show a smaller spread between ensemble members, and accordingly, a higher robustness of the PPC_{prob} fields.

Finally, the vertical moisture flux is significantly higher on the non-robust days than on the robust days. While this quantity is primarily influenced by the overall higher specific humidity q due to higher air temperatures during the summer months, this illustrates that lifting motion in the summer months transports substantially more moisture into the upper troposphere. Consequently, a small difference in the vertical velocity value causes a large resulting change in vertical moisture flux, which could be one of the reasons for the uncertainties in the ensemble predictions. Generally, estimating the vertical motion in the atmosphere presents a challenge for NWP models, as the order of magnitude of vertical motion is much smaller than for horizontal motion (Holton & Hakim, 2012).

7. Conclusion and Outlook

In this Master thesis, PPC- and PPC_{prob}-forecasts derived from the ICON deterministic (PPC) and ensemble (PPC_{prob}) weather forecasts are analyzed. There is a significant seasonal pattern in the median of the conditional distribution $f(PPC_{prob} \mid PPC = 1)$, with lower values in the summer months and higher values occurring in the winter months. Although the absolute areas where the ensemble and the deterministic forecasts disagree (as identified by a threshold-based method) show a reverse seasonal pattern, with the absolute area of false positive forecasts occurring in the winter months, the relative uncertainty area, which is a more relevant factor for the forecast of individual ISSRs follow the general seasonal pattern of the median $f(PPC_{prob} \mid PPC = 1)$. Ten days with a high median $f(PPC_{prob} \mid PPC = 1)$ (robust days) and ten days with a low $f(PPC_{prob} \mid PPC = 1)$ (non-robust days) were chosen for further analysis.

On these selected days, a majority of the ISSRs occur in the proximity to frontal systems. Generally, on the robust days, the atmosphere is characterized by stronger geopotential gradients, higher geostrophic wind velocities and ISSRs have a larger horizontal extent. On the non-robust days, the atmosphere appears less organized, i.e., geopotential gradients and geostrophic winds are weaker and ISSRs are more fragmented and smaller in scale. False positives and false negatives occur predominantly near the boundaries of ISSRs on robust, while on non-robust days, they are additionally interspersed with ISSRs.

The results suggest that the robustness of the forecast of regions where persistent contrails form is closely linked to the horizontal extent of the areas where the model predicts PPC = 1, which can be inferred from the high correlation between the median of the conditional distribution of $f(PPC_{prob} \mid PPC = 1)$. On days where the MCL is low, there is a lower agreement between the deterministic run and the ensemble runs than on days with a high MCL.

One explanation for the different length scales on days where the forecast is more robust compared with the days where the forecasts is less robust is that ISSRs on these days are formed by different mechanisms. The robust days are associated with strong geostrophic winds and large-scale lifting, which indicates only little mixing. Relative humidity increases are mainly driven by cooling. The non-robust days, on the other hand, days characterized by weaker geopotential gradients and, on average, less lifting, both within ISSRs and in the 24-hours trajectories. Notably though, strong uplift

(< -1 Pa s^{-1}) could be identified in the trajectories about twice as often on the non-robust days than on the robust days. Additionally, trajectories pass through regions that were characterized by a high vertical moisture flux integrated over twenty-four hours and the increases in relative humidity were associated with increases in specific humidity. This indicates that more mixing in the flow occurred on the non-robust days. These findings suggest that the dominating formation process on the non-robust days is of convective nature, while gradual ascents along ridges is the prevalent driver for ice supersaturation on the robust days. Finally, the overall lower temperatures during the winter months, when all the robust days occur generally promote ice supersaturation even though the air masses' specific humidity does not substantially increase. This is because at low temperature, relative humidity becomes more sensitive to temperature changes due to the exponential behavior of the saturation vapor pressure w.r.t. ice.

A limitation of this study is that due to computational constraints and data availability, the backwards trajectories could only be calculated only along one pressure level and only over 24 hours. In other words, lifting processes, which occur in both convective (as rapidly rising air) and frontal processes (as generally smoother, large-scale ascent), are inhibited per the design of the experiment. Additionally, the trajectories were calculated using a single-step Eulerian scheme. These limitations could be removed by further investigating air parcels that terminate in ISSRs in a dedicated Lagrangian trajectory model, e.g., FLEXPART (Stohl et al., 2005).

Furthermore, it proved quite difficult to identify deep convective activity based solely on the magnitude of the vertical velocities. For instance, even on one of the days where observational data proved that thunderstorms were present, the maximum velocity derived from the ERA5 reanalysis and ICON forecast data at 250 hPa were only -1.52 Pa/s and -2.80 Pa/s, respectively. This is because of spatial and temporal averaging and the general difficulty in accurately representing sub-grid, turbulent processes in computer models. Deep convection is not only characterized by extreme updrafts but also by downdrafts that occur in close proximity (Wallace & Hobbs, 2006). About 80% of the moisture that condenses in the updraft of thunderstorms does not reach the ground as precipitation but either evaporates or remains in the upper troposphere as remnants of cirrus anvils (Wallace & Hobbs, 2006). One study found a strong correlation between global lightning intensity and high-level cirrus cover with a time lag of three days (Saha et al., 2023). This illustrates that the vast amounts of moisture injected into the upper troposphere can facilitate the formation of cirrus clouds, even days after a thunderstorm has occurred. Further research could therefore involve other parameters used in the forecast of deep convective activity, e.g., convective available potential energy (CAPE, Wallace & Hobbs, 2006).

It should be noted that this study relies solely on data derived from numerical models and no validation against observational data was performed. To improve any contrail avoidance strategies, observational data, e.g., from satellite imaging could be used to supplement NWP output.

Finally, to answer the three research questions:

1. Are there synoptic situations during which the forecast of ISSRs is especially robust or not?

Yes, the forecast of ISSRs was found to be especially robust on winter days with strong geopotential gradients, strong geostrophic winds and low temperatures in the upper troposphere. The forecast of ISSRs on summer days following deep convective events was found to be less robust.

2. Are there any synoptic situations where one can confidently say that the application of operational contrail avoidance strategies (e.g., rerouting air traffic to avoid ISSRs) is particularly beneficial to the overall climate impact of aviation?

Yes, robust forecasts in the winter months coincide with shorter days, on which contrails generally have a stronger warming effect due to shorter daytime. Therefore, focusing on winter days with strong geopotential gradients makes sense for the trial of new contrail avoidance strategies.

3. Which (if any) practical conclusions can be drawn for possible contrail avoidance strategies for flight dispatchers and pilots?

Generally, the findings that forecasts of ISSRs in the winter months are more robust than in the summer months is quite useful for operational contrail avoidance as the overall lower traffic volume in the winter likely makes their implementation easier. Summer months, on the other hand, are characterized by an overall higher volume of traffic, which increases both air traffic controllers' and pilots' workloads. Days on which thunderstorms occur pose an additional challenge, as ATC sectors are often regulated in these cases to facilitate thunderstorm avoidance.

References

Ahrens, C. D., & Henson, R. (2022). *Meteorology today : an introduction to weather, climate and the environment*. Cengage.

von Bonhorst, G., Maizet, M., & Gierens, K. (2025). On contrail prediction under realistic weather forecast uncertainty using the example of WAWFOR data. *Meteorologische Zeitschrift*. https://doi.org/10.1127/metz/1251

Brannan, J. R. ., Boyce, W. E. ., & McKibben, M. A. . (2015). *Differential equations : an introduction to modern methods and applications*. Wiley.

Copernicus Climate Change Service. (2025). Climate Data Store. Retrieved from https://cds.climate.copernicus.eu

DWD. (2025a). Analyse- und Prognosekarten Europa. Retrieved from https://www.dwd.de/DE/leistungen/hobbymet_wk_europa/hobbyeuropakarten.html#buehneTop

DWD. (2025b, September 25). Pamore - Retrieving archived forecast model data.

DWD. (2025c, September 28). WAWFOR data set for aviation.

Gierens, K., & Spichtinger, P. (2000). On the size distribution of ice-supersaturated regions in the upper troposphere and lowermost stratosphere. *Annales Geophysicae*, *18*(4), 499–504. https://doi.org/10.1007/s00585-000-0499-7

Gierens, K. (2010). Contrails and contrail cirrus. In *Encyclopedia of aerospace engineering* (Vol. 48, pp. 48-4831-48–4831). https://doi.org/10.5860/choice.48-4831

Gierens, K., Spichtinger, P., & Schumann, U. (2012). Ice Supersaturation (pp. 135–150). https://doi.org/10.1007/978-3-642-30183-4_9

Gierens, K., Wilhelm, L., Hofer, S., & Rohs, S. (2022). The effect of ice supersaturation and thin cirrus on lapse rates in the upper troposphere. *Atmospheric Chemistry and Physics*, *22*(11), 7699–7712. https://doi.org/10.5194/acp-22-7699-2022

Hanst, M., Köhler, C. G., Seifert, A., & Schlemmer, L. (2025). Predicting ice supersaturation for contrail avoidance: ensemble forecasting using ICON with two-moment ice microphysics. *Atmospheric Chemistry and Physics*, *25*(23), 17253–17274. https://doi.org/10.5194/acp-25-17253-2025

Hersbach, H., Bell, B., Berrisford, P., Biavati, G., Horányi, A., Muñoz Sabater, J., et al. (2023). ERA5 hourly data on single levels from 1940 to present. https://doi.org/10.24381/cds.adbb2d47

Hofer, S., Gierens, K., & Rohs, S. (2024). How well can persistent contrails be predicted? An update. *Atmospheric Chemistry and Physics*, *24*(13), 7911–7925. https://doi.org/10.5194/acp-24-7911-2024

Hofer, S. M., & Gierens, K. (2025). Synoptic and microphysical lifetime constraints for contrails. *Atmospheric Chemistry and Physics*, *25*(16), 9235–9247. https://doi.org/10.5194/acp-25-9235-2025

Holton, J. R., & Hakim, G. J. (2012). *An introduction to dynamic meteorology: Fifth edition* (Vol. 88). https://doi.org/10.1016/C2009-0-63394-8

IEA. (2025, January 16). Aviation.

Lee, D. S., Fahey, D. W., Skowron, A., Allen, M. R., Burkhardt, U., Chen, Q., et al. (2021). The contribution of global aviation to anthropogenic climate forcing for 2000 to 2018. *Atmospheric Environment*, *244*. https://doi.org/10.1016/j.atmosenv.2020.117834

Martin, J. E. (2013). *Mid-latitude atmospheric dynamics: a first course*. John Wiley & Sons.

Matthes, S., Gierens, K., Beckmann, B., Bugliaro, L., Dietmüller, S., Frömming, C., et al. (2026, February 17). D-KULT: data and tools for routine eco-efficient flight operations. https://doi.org/10.5194/jecats-2026-3

Müller, G., & Floors, R. (2025). Wetterzentrale. Retrieved from https://wetterzentrale.de/

Myhre, G., Shindell, D., Bréon, F.-M., Collins, W., Fuglestvedt, J., Huang, J., et al. (2014). Anthropogenic and natural radiative forcing. *Climate Change 2013-The Physical Science Basis*, 659–740.

Reinert, D., Prill, F., Frank, H., Denhard, M., Baldauf, M., & ... (2020). *DWD database reference for the global and regional ICON and ICON-EPS forecasting system. … Online: Https://Www. Dwd …*. Retrieved from https://www.dwd.de/DWD/forschung/nwv/fepub/icon_database_main.pdf

Saha, J., Price, C., & Guha, A. (2023). The role of global thunderstorm activity in modulating global cirrus clouds. *Geophysical Research Letters*, *50*(12), e2022GL102667.

Sausen, R., Hofer, S., Gierens, K., Bugliaro, L., Ehrmanntraut, R., Sitova, I., et al. (2024). Can we successfully avoid persistent contrails by small altitude adjustments of flights in the real world? *Meteorologische Zeitschrift*, *33*(1). https://doi.org/10.1127/metz/2023/1157

Schuh, H. Z., Reutter, P., Niebler, S., & Spichtinger, P. (2025, July 18). Fractal Characteristics of Ice-Supersaturated Regions in the Tropopause Region of the northern midlatitudes. https://doi.org/10.5194/egusphere-2025-2498

Schumann, U. (1996). Über Bedingungen zur Bildung von Kondensstreifen aus Flugzeugabgasen. *Meteorologische Zeitschrift*, *5*(1), 4–23. https://doi.org/10.1127/metz/5/1996/4

Schumann, U., & Seifert, A. (2025). On the Weather Impact of Contrails: New Insights from Coupled ICON–CoCiP Simulations. *Atmospheric Chemistry and Physics*, *25*(24), 18571–18597. https://doi.org/10.5194/acp-25-18571-2025

Spichtinger, P., & Leschner, M. (2016). Horizontal scales of ice-supersaturated regions. *Tellus B: Chemical and Physical Meteorology*, *68*(1), 29020. https://doi.org/10.3402/tellusb.v68.29020

Spichtinger, P., Gierens, K., & Wernli, H. (2005). A case study on the formation and evolution of ice supersaturation in the vicinity of a warm conveyor belt’s outflow region. *Atmospheric Chemistry and Physics*, *5*(4), 973–987.

Stocker, T. (2014). *Climate change 2013: the physical science basis: Working Group I contribution to the Fifth assessment report of the Intergovernmental Panel on Climate Change*. Cambridge university press.

Stohl, A., Forster, C., Frank, A., Seibert, P., & Wotawa, G. (2005). Technical note: The Lagrangian particle dispersion model FLEXPART version 6.2. *Atmospheric Chemistry and Physics*, *5*(9). https://doi.org/10.5194/acp-5-2461-2005

Teoh, R., Schumann, U., Majumdar, A., & Stettler, M. E. J. (2020). Mitigating the

Climate Forcing of Aircraft Contrails by Small-Scale Diversions and Technology Adoption. *Environmental Science & Technology*, *54*(5), 2941–2950. https://doi.org/10.1021/acs.est.9b05608

Wallace, J. M., & Hobbs, P. V. (2006). *Atmospheric Science: An Introductory Survey: Second Edition*. *Atmospheric Science: An Introductory Survey: Second Edition*. https://doi.org/10.1016/C2009-0-00034-8

Wilhelm, L., Gierens, K., & Rohs, S. (2021). Weather Variability Induced Uncertainty of Contrail Radiative Forcing. *Aerospace*, *8*(11), 332. https://doi.org/10.3390/aerospace8110332

Wilhelm, L., Gierens, K., & Rohs, S. (2022). Meteorological Conditions That Promote Persistent Contrails. *Applied Sciences*, *12*(9), 4450. https://doi.org/10.3390/app12094450

Wolf, K., Bellouin, N., Boucher, O., Rohs, S., & Li, Y. (2025). Correction of ERA5 temperature and relative humidity biases by bivariate quantile mapping for contrail formation analysis. *Atmospheric Chemistry and Physics*, *25*(1), 157–181. https://doi.org/10.5194/acp-25-157-2025

WxFUSION. (2023). *REAL-TIME THUNDERSTORM HAZARD INFORMATION FOR TURBULENCE AVOIDANCE AND OPTIMIZED ROUTING*.

List of Figures

Figure 1: Mixing trajectories for two different exhaust plumes (dashed lines). The slopes of the mixing trajectories are given by G. The curves indicate the water vapor saturation partial pressure w.r.t. water (upper curve) and ice (lower curve). A parcel of air from one of the two exhaust plumes originates at the top right (outside of the plotted region) and, during the mixing with ambient air, travels along the mixing trajectory. Contrail formation occurs if the parcel becomes transiently (super-)saturated w.r.t. liquid water, i.e., if the mixing trajectory at least tangentially touches or intersects the upper curve. For contrails to persist, the ambient atmospheric conditions must lie in the darkly shaded grey region. In contrast, in the lightly shaded grey region, RH_{ice} < 100% and contrails will evaporate. Figure taken from Gierens, 2010. 10

Figure 2: Region considered in this study (i.e., the ICON EU model domain, marked by the red outline) with all possible starting points for the Lagrangian backwards trajectories, denoted by the “x” markers. The starting points for the trajectories were chosen from the locations where PPC = 1. 24

Figure 3: Daily median (black), Q1-Q3 range (shaded in grey), standard deviation (light blue) and the proportion of the conditional distribution f(PPC_{prob} | PPC = 1) and the proportion of all grid cells where PPC = 1 as a measure for the overall ice supersaturation ($n_{PPC=1}$/n, where n is the number of grid cells, green) for the 12:00 h forecast with a lead time of 01h (left) and the 00:00 h forecast with a lead time of 13h. 26

Figure 4: Boxplot of the conditional distribution PPC_{prob} | PPC = 1 for the four different seasons for the 12:00 + 01:00h forecast (blue) and the 00:00 + 13:00h forecast (green). The box indicates the range between the first and third quartile, the horizontal blue and green lines in the boxes represent the median and the whiskers indicate the 1.5 interquartile range (IQR). Outliers are not shown. 27

Figure 5: Daily MCL and median PPC_{prob} | PPC = 1 (left). MCL calculated over the entire timeseries and the Pearson correlation coefficient between MCL and the median PPCprob | PPC = 1 for each pressure level (right). The results are displayed for the 12:00 + 01:00 h forecast. 29

Figure 6: Receiver operating characteristics (ROC) curve for the 12:00 + 00:01 h and 00:00 + 13:00 h forecast (left) for different values of k ∈ {0.0, 0.1, 0.2, …, 1.0} and the Youden Index (right). 30

Figure 7: PPC and PPCprob fields on June 01st, 2024, one of the non-robust days for FL340 (250 hPa, a) and FL300 (300.9 hPa, d), on January 01st, 2025 (p = 250 hPa, b, p = 300.9 hPa, e), one of the robust days with a zonal pattern, and on January 12th, 2025 (p = 250 hPa, c, p = 300.9 hPa, f), one of the robust days with a blocking pattern. Grey areas indicate true positives (PPC = 1 and PPC_{prob} > 0.3), orange areas indicate false positives (PPC = 0 and PPC_{prob} > 0.3) and light blue areas indicate false negatives (PPC = 1 and PPC_{prob} < 0.3). The solid black lines indicate the normalized geopotential. 30
Figure 8: Autocorrelation length of the vertical velocity (OMEGA), relative humidity (RELHUM) and temperature fields for the 12:00 + 01:00 h forecast from the PAMORE dataset for the 200, 250 and 300 hPa pressure levels (FL390, FL340 and FL300, respectively) for the robust days. The median of the respective distribution is indicated by the red line. In each subplot, ten days of 27 latitude bands are plotted, giving a total of 270 lines per plot. 32
Figure 9: As for figure 8 but for the non-robust days. 33
Figure 10: Histogram of the distribution of the autocorrelation scale of the vertical velocity for the robust and non-robust days in a log-log plot and the cumulative distribution function for both distributions (CDF, right). 33
Figure 11: Synoptic situation at p = 250 hPa on June 01st, 2024 (left) as an example for one of the non-robust days, January 01st, 2025 (center), one of the robust days with a zonal pattern and January 12th, 2025 (right), one of the robust days with a blocking pattern. The shaded regions indicate areas where PPC=1, the solid lines are lines of equal normalized geopotential. 34
Figure 12: Cumulative distributions of lapse rates on robust (R) and non-robust (NR) days (left) for regions where PPC = 1 and regions where PPC = 0, and histograms of the lapse rate distributions on robust (center) and non-robust days (right), both for regions where PPC = 1 and PPC = 0. 35
Figure 13: Sample trajectories for three robust day (top row) and three non-robust days (bottom row) each. The black lines indicate the individual trajectories. Grey shaded regions indicate the ERA5 PPC = 1 regions, derived from ERA5 temperature and relative humidity on the relevant day at 13:00 h UTC. The blue and red regions denote the integrated vertical moisture flux in the 24 hours prior to 13:00 h UTC on the relevant day. 36

Figure 14: Histograms of the relative humidity (left), vertical velocity (center) and vertical moisture flux (right) of all trajectories calculated on the non-robust days (grey) and on the robust days (light blue). The vertical lines indicate the median of the respective dataset. The histograms for all six distributions were calculated with n = 50 bins...37
Figure 15: Evolution of temperature (left), relative humidity (center) and specific humidity (right) in the trajectories over the 24 hours prior to the 13:00 h UTC on the robust (blue) or non-robust (red) days. The very thin red and blue lines are the values for each trajectory, while the blue and red boxes indicate the median of all trajectories in the subset robust or non-robust days. The median values of the temperature, relative and specific humidity shown here differ from the median values of the difference that the individual air parcels experience. This is because not all trajectories have the same length. If an air parcel is outside of the model boundary at that time step, it is not considered in this plot. For instance, a trajectory with a temperature decrease of 3 °C over 24 hours will have a much shallower slope than a trajectory with the same temperature decrease over only six hours. 38
Figure 16: Scatterplot of all the temperature and specific humidity changes of all trajectories on the robust (blue) and non-robust days (red, left), where the squared markers indicate the median of both subset and histograms for the temperature (center) and specific humidity changes (right) for both subset of days (robust blue, non-robust grey). 39
Figure 17: The annual cycle of the uncertainty ration ((FP+FN)/TP) and the median f(PPC_{prob} | PPC = 1). The triangles (circles) indicate the respective values on the robust (non-robust days). 41
Figure 18: Satellite image (left) of the convective situations on at 13:04 h UTC (the figure was kindly provided by WxFUSION GmbH) vertical velocities at p = 250 hPa from the ICON forecast data (12:00 h UTC + 01:00, center) and ERA5 reanalysis data (13:00, right) on 22.07.2024, one of the non-robust days. The magenta areas in the satellite image indicate active thunderstorms that were identified as they coincide with measured lightning activity and rapid cloud growth. 45
Figure 19: ERA5 (left) and ICON (right) vertical velocities at p = 250 hPa at 13:00 h UTC on 12.01.2025, one of the robust days. 46
Figure 20: Surface analysis at 00:00 h UTC on 12.01.2025 of the DWD ((c) DWD, retrieved from Wetterzentrale.de (left, (c) DWD, 2025a, retrieved from Müller & Floors,

2026) and the wind speed and normalized geopotential height at p = 250 hPa for the 12:00 h UTC + 01:00 h forecast on 12.01.2025 (right). The stippled regions indicate PPC = 1. 46

List of Tables

Table 1: Flight levels and the corresponding pressure levels used in this study. 13

Table 2: Contingency table for PPC_{ens} and PPC. 19

Table 3: Statistical properties of selected properties of the Lagrangian trajectories for the robust (R) and non-robust (NR) days. 37